CHEMMEDCHEM

CHEMISTRY ENABLING DRUG DISCOVERY

Accepted Article

Title: PET imaging of T cells: Target identification and feasibility assessment

Authors: Yves P. Auberson, Emmanuelle Briard, Bettina Rudolph, Klemen Kaupmann, Paul Smith, and Berndt Oberhauser

To be cited as: *ChemMedChem* 10.1002/cmdc.201800241

Link to VoR: http://dx.doi.org/10.1002/cmdc.201800241

A Journal of

ChemPubSoc Europe

WILEY-VCH

www.chemmedchem.org

PET imaging of T cells: Target identification and feasibility assessment

Dr. Yves P. Auberson,*[a] Dr. Emmanuelle Briard,[a] Dr. Bettina Rudolph[b], Dr. Klemens Kaupmann,[a] Dr. Paul Smith,[c] and Dr. Berndt Oberhauser[a]

[a] Dr. Y. P. Auberson, Dr. E. Briard, Dr. B. Oberhauser, Dr. K. Kaupmann
Global Discovery Chemistry
Novartis Institutes for BioMedical Research
141 Klybeckstrasse, 4057 Basel, Switzerland
E-mail: yves.auberson@novartis.com
[b] Dr. B. Rudolph
Translational Medicine, Pharmacokinetics Sciences
Novartis Institutes for BioMedical Research
141 Klybeckstrasse, 4057 Basel, Switzerland
[c] Dr. P. Smith
Autoimmunity, Transplantation & Inflammation
Novartis Institutes for BioMedical Research
Novartis Campus, 4056 Basel, Switzerland

Abstract: Imaging T cells using positron emission tomography (PET) would be highly useful for diagnosis and monitoring in immunology and oncology patients. There are however no obvious targets that can be used to develop imaging agents for this purpose. We evaluated several potential target proteins with selective expression in T cells, and for which lead molecules were available: PKC θ, Lck, ZAP70 and Itk. Ultimately, we focused on Itk (interleukin-2-inducible T cell kinase) and identified a tool molecule with properties suitable for in vivo imaging of T cells, (5a*R*)-5,5-difluoro-5a-methyl-N-(1-((*S*)-3-(methylsulfonyl)-phenyl)(tetrahydro-2*H*-pyran-4-yl)methyl)-1*H*-pyrazol-4-yl)-1,4,4a,5,5a,6-hexahydro-cyclopropa[*f*]-indazole-3-carboxamide (**23**). While not having the optimal profile for clinical use, this molecule indicates that it might be possible to develop Itk-selective PET ligands for imaging the distribution of T cells in patients.

Introduction

Improved tools for imaging T cells and quantifying their organ distribution would be highly useful for diagnosis and monitoring disease progression in cancer and immune diseases. They would open the door to more effective clinical stratification methods, and allow monitoring of the therapeutic efficacy of drugs acting on pathways associated with T cell activity. They would facilitate the selection of clinically effective doses, and inform on changes in the distribution of T cells in organs that are not readily accessible for sampling.

T cells are a subtype of lymphocytes and play a central role in cell-mediated immunity. They are divided in several classes including helper, killer, memory and regulatory T cells, depending on their specific function in the immune system. Besides their protective role, T cells are implicated in a diverse set of illnesses, including autoimmune, inflammatory and allergic diseases. The options for monitoring T cells *in vivo*, beyond measuring their concentration in blood samples, are currently limited. In clinical practice, T cell activity is mostly determined from blood samples or biopsies.

Positron Emission Tomography (PET) is a non-invasive imaging technique, often used in combination with Magnetic Resonance Imaging (MRI) or X-ray based Computer Tomography (CT) for enhanced spatial resolution. In allows diagnosis and monitoring of disease progression, and is most frequently used for imaging of tumors, brain and cardiac diseases. PET delivers molecular and functional information according to the applied tracer and its biological target. Most PET tracers have been developed for imaging targets in the brain,[1] or for diagnosing tumors and monitoring therapy in cancer patients.[2] They provide valuable information on target expression in health and disease, or about target engagement by drug candidates, facilitating the selection of optimized therapeutic doses. In contrast, there are very few tracers available for receptor occupancy studies in peripheral tissues.[3]

In oncology, the most frequently used tracer are [^{18}F]-fluorodeoxyglucose ([^{18}F]FDG) and [^{18}F]-fluorothymidine ([^{18}F]FLT), which provide valuable information on tumor metabolism. While largely accepted as biomarkers of tumor activity, both [^{18}F]FDG and [^{18}F]FLT have limitations, including the fact that they do not differentiate well between cancer and inflammation.[4] Novel T cell-specific imaging agents that could be used in peripheral organs would effectively support diagnosis and evaluation of drug candidates in immuno-oncology.[5] They would also greatly facilitate the therapeutic development of cell-based therapies such as chimeric antigen receptor (CAR) T cells[6]

In immunology, there are few tracers that can be used to monitor disease, or to follow immune cell populations in patients. Tracers allowing the detection of activated microglia by targeting the translocator protein (TSPO)[7] are an exception. The prototypical TSPO tracer is [^{11}C]-PK11195.[8] While suffering from a relatively low signal-to-noise ratio, it is nevertheless used for quantifying inflammatory responses in various organs.[9] Second-generation tracers such as [^{11}C]-PBR28,[10] while displaying improved properties, are sensitive to a single TSPO polymorphism (rs6971) that strongly degrades their performance in a portion of human patients.[11] Recently, novel tracers binding to the purinergic receptor subtype 7 (P2X7R), have shown promise as tools for imaging inflammation.[12] P2X7R are expressed on cellular membranes of myeloid-derived cells and have also been implicated in mediating microglial proliferation at the site of injury.

There are no low-molecular weight (lmw) tracers for T cells, but monoclonal antibodies directed against CD4- or CD8-positive T cells have been shown to allow imaging of lymph nodes and spleen with high specificity in mice.[13] In the clinic, one study with radiolabeled anti-CD4 antibodies demonstrated positive results in rheumatoid arthritis.[14] The use of antibody-based imaging agents is however limited by the comparatively high radioactive load associated with the long-lived radioisotopes required for their labeling (e.g. ^{89}Zr), by the slow kinetics of their organ distribution, and by their inability to penetrate the blood-brain barrier.[13,15] A broad and rapid distribution of the imaging agent in all organs would indeed be important for imaging T cells in the brain and spinal cord (in multiple sclerosis), in salivary glands (for Sjögren's disease), in muscles (for myositis), pancreas (in diabetes), in the intestine (coeliac disease), in the lung (sarcoidosis) or in the thyroid (autoimmune thyroiditis).

Our aim was to develop a low molecular weight PET tracer for imaging T cells in peripheral organs, and potentially also in the brain. The first task was to identify candidate cellular targets for developing selective imaging agents, and the corresponding chemical starting points for PET tracer optimization.

Target selection process

The first step for the selection of suitable targets was the screening of several RNA expression databases for target proteins fulfilling the following criteria: differential expression in T cell derived cell lines vs. other immunocytes, selective expression in T cells isolated from blood[16] as well as a pronounced expression in T cell rich organs[17] like spleen, thymus and lymph nodes. For a limited number of targets, mass spectroscopy-based protein expression data has also been published,[18] providing an additional source of data for selection.

Imaging probes for targets expressed across all T cell classes have the potential for being useful in a variety of clinical settings, addressing both the regulatory role as well as the effector function of T cells in immunological disorders. We therefore did not include criteria that would restrict our selection to targets providing T cell subtype-specificity, i.e. leading to lmw tracers capable of discerning between different cellular T cell subpopulations. In contrast, we focused on targets described to have similar mRNA expression levels across the major T cell subpopulations.

In the second stage of target selection, we focused on the availability of potent and specific lmw lead molecules, either from our proprietary compound collection or from the literature. Information on the target structure-activity-relationship (SAR) and selectivity profile of the chemical series, when available, greatly facilitated prioritization.

From a medicinal chemistry point-of-view, we carefully considered information on the potential to modulate physico-chemical properties, non-specific binding, metabolism, and the pharmacokinetic profile of the chemical leads. The characteristics of successful PET tracers have been extensively discussed in the literature,[19, 20] with an emphasis on tracers for the central nervous system (CNS). Tracers for peripheral applications face the additional challenge resulting from the signal generated by radio-metabolites produced *in vivo*, and which can potentially interfere with the signal related to the parent tracer. Finally, we considered options to introduce a PET radioisotope on the tracer candidate, at a late stage of its chemical synthesis, as an essential factor for the feasibility of the approach.

The conclusion of this selection process showed that T cell receptor subunits, co-stimulatory receptors and components of the associated signaling pathways, as well as the corresponding transcription factors constitute the most T cell specific targets. There was however no suitable starting point available for the optimization of lmw ligands for these targets.

In addition, a few function-related proteins were identified, and these were mostly associated to cytotoxic T cells. Proteins like protease Granzyme K, which are involved in the T cell response, might reach high expression levels during inflammation and therefore be good target candidates for imaging. We however did not identify selective chemical starting points for the optimization of PET tracers for these targets either.

Our focus therefore shifted towards T cell specific intracellular signaling pathway components, of which receptor proximal kinases proved to be the most cell type specific. Intracellular targets come with a requirement for cell penetration, which is a challenge for antibodies and other biological agents. In contrast, lmw tracer candidates generally penetrate cells rapidly, allowing the evaluation of targets otherwise not exploitable for imaging. Naturally, these signaling nodes also represent promising pharmacological targets for immunological indications, which allowed us to mine the target profiles of a variety of published and proprietary inhibitors from very diverse chemical series.

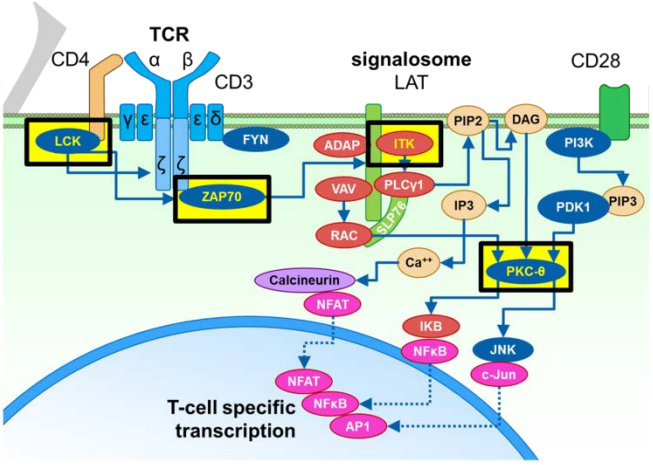

Scheme 1. Simplified T-cell signalling pathways with the selected radioligand targets highlighted: Lck and ZAP70 are directly associated with the T-cell receptor complex, Itk is linked to the signalosome and the downstream signal transducer PKC θ.

In the majority of the kinase families of interest, only one of the isoforms has the necessary T cell specificity. The fact that these isoforms display a high degree of sequence similarity, especially in the active sites, poses a formidable challenge to the development of selective PET tracer candidates. For example, amongst the closely related members of the Tec-kinase family Txk, Btk, Bmx and Tec show also high mRNA levels in B cells,

mast cells and the monocytic lineage, leaving only Itk as a truly T-cell specific target. We thus selected kinases from the T cell receptor signaling cascade and co-stimulatory pathways, including Zap70, PKC θ, Lck and Itk (Scheme 1, Table 1) for further evaluation of available chemical starting points.

Table 1. Expression profile of Itk, Lck, PKC θ and ZAP70 in the immune compartment.

Tissue	Itk[a]	Lck[b]	PKC θ [c]	ZAP70[d]
$CD4^+$ T cells	+++	+++	+++	+++
$CD8^+$ T cells	+++	+++	+++	+++
NK cells	+	+/-	+	++
DCs	-	-	-	+
B cells	-	+/-	-	-
Non-immune tissues	-	retina	retina, testis, muscle	liver

[a] Tyrosine-protein kinase Itk/Tsk, also known as interleukin-2-inducible T cell kinase; [b] lymphocyte-specific protein tyrosine kinase; [c] protein kinase C, isozyme θ; [d] zeta-chain-associated protein kinase 70.

Results and Discussion

Chemistry

1. PKC θ inhibitors

The synthetic route toward compound **4** is shown in Scheme 2. Catalytic hydrogenation of 2,2,2-trifluoro-1-(pyrazin-2-yl)ethan-1-one (**1**) over platinum oxide led to 1,1,1-trifluoro-2-(piperazin-2-yl)propan-2-ol (**2**), which under basic conditions reacted with substituted butyldimethylsilyl-pyridine **3**[21] to afford the target product.

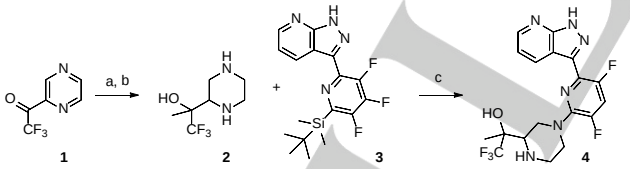

Scheme 2. Synthesis of PKC θ inhibitor **4**. *Reagents and conditions:* a) $(CH_3)_3SiCF_3$, K_2CO_3, DMF, RT, 12 h, 60%; b) PtO_2, MeOH, H_2, 4 bar, RT, 24 h, quant.; c) Hunig's base, NMP, 150°C, MW, 2 h, 30%.

2. LCK inhibitors

Scheme 3 shows the preparation of LCK inhibitor **9** from the previously known mesylate **5**.[22] Treatment with commercially available 3-iodo-1H-pyrazolo[3,4-d]pyridine-4-amine in presence of potassium carbonate led to the formation of compound **6**. Deprotection and reprotection with the more labile Boc group provides intermediate **7**, which reacted with boronate **8**[23] to produce the desired product.

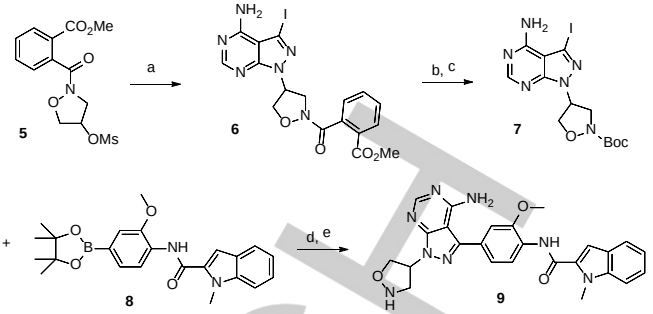

Scheme 3. Synthesis of LCK inhibitor **9**. *Reagents and conditions*: a) 3-iodo-1H-pyrazolo[3,4-d]pyridine-4-amine, K_2CO_3, DMF, 90°C, 16 h, quant.; b) 4M HCl, 100°C, 16 h, quant.; c) Boc anhydride, Et_3N, CH_2Cl_2, RT, 16 h, 38%; d) **8**, $Pd(dppf)Cl_2$, K_2CO_3, DMSO, 95°C, 1.2 h, quant.; e) HCl 4M in dioxane, RT, 18 h, 24%.

3. ITK inhibitors

Scheme 4 shows the assembly of the tetrahydroindazole Itk inhibitors (±)**14**, **15a** (eutomer) and **15b** (distomer). Intermediate **11** was prepared by reducing phenyl(piperidin-4-yl)methanone **10** to a racemic carbinol, conversion to a benzylic chloride and alkylation of 4-nitropyrazole, followed by reduction of the nitro group with Zn/NH_4Cl. Subsequent coupling with the carboxylic acid **12** provided **13**. Deprotection of the piperidine, optional alkylation with fluoroiodoethane and deprotection of the indazole provided the desired products. The enantiomers of **15** were separated by chiral chromatography.

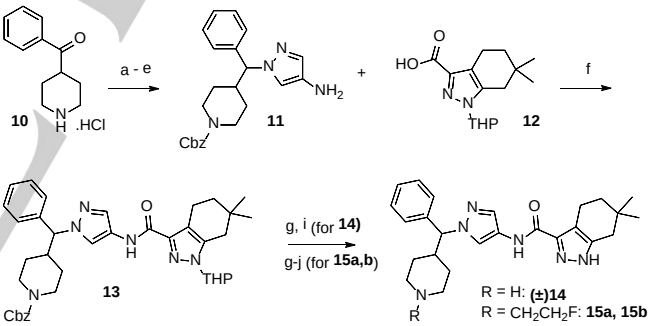

Scheme 4. Synthesis of Itk inhibitors (±)**14**, **15a**, **15b**. *Reagents and conditions:* a) Cbz-Cl, K_2CO_3, THF, 0-25°C, 15 h; b) $NaBH_4$, MeOH, 0-25°C, 15 h; c) $SOCl_2$, DCM, RT, 15 h; d) 4-nitropyrazole, K_2CO_3,KI, DMF, 100°C, 15 h; e) Zn, NH_4Cl, THF/water f) HATU, DIPEA, DMF, 50°C, 4 d; g) Pd/C, H_2, MeOH, RT, 4 h; h) 1-fluoro-2-iodoethane, K_2CO_3, DMF, RT, 15 h; i) HCl/dioxane, RT, 15 h; j) chiral prep HPLC (CHIRALPAK® IA, eluent: n-hexane, 0.1% DEA in EtOH).

The difluorocyclopropyl-constrained tetrahydroindazole **18** (Scheme 5) was prepared analogously, via the THP protected racemic acid **17**[24]. The four stereoisomers were separated by chiral HPLC; the biochemical potency of the most potent stereoisomer (exact configuration not determined) is reported.

Racemic **19**[25] and **20**[24] were synthesized according to literature, and obtained optically pure after chiral separation as described in the experimental part (Scheme 6). Amide coupling led to thioether **21**, which was then oxidized to the sulfoxide **22** using t-BuOOH in decane**.**

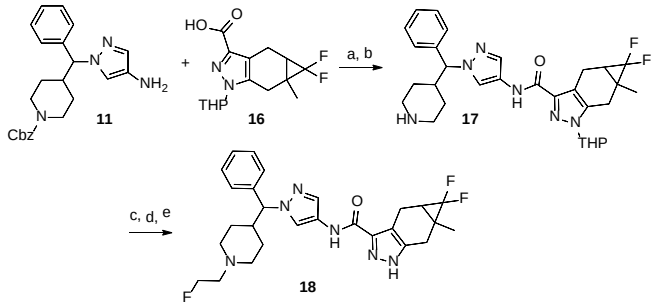

Scheme 5. Synthesis of Itk inhibitor **18**. *Reagents and conditions:* a) BOP, DIPEA, DMF, RT, 48 h; b) Pd-C, H_2, EtOH, RT, 6 h; c) 1-fluoro-2-iodoethan, K_2CO_3, DMF, 80°C, 48 h; d) HCl/dioxane, RT, 15 h. e) chiral prep HPLC.

The stereoisomers resulting from the formation of the sulfoxide could be separated by chiral HPLC, and the biological data is given for the more active diastereoisomer. All four stereoisomers of **23** were obtained after coupling of racemic **19** and **20** and oxidation of the thioether with mCPBA. They were separated by chiral chromatography. The isomer with the highest potency in the biochemical assay was selected for *in vivo* characterization.

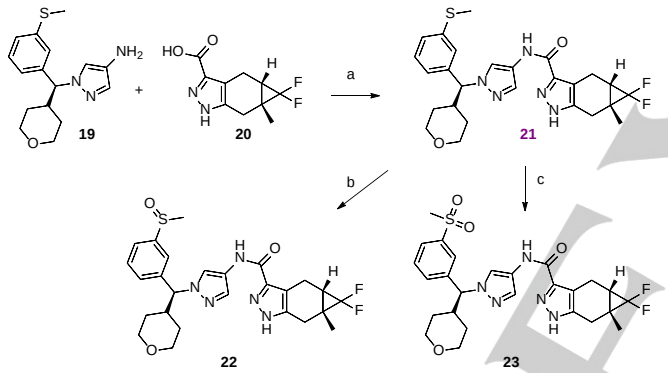

Scheme 6. Synthesis of Itk inhibitors **22** and **23**. *Reagents and conditions*: a) BOP, DMF, 50°C, 4 h; b) t-BuOOH 6M in decane, RT, 2 h; c) mCPBA, DCM, 0°C, 1 h.

For the preparation of radiolabeled [$^3H_2$]-**23** (Scheme 7), two bromine atoms were introduced on the benzene and pyrazole rings of **21** to provide **24**. X-ray analysis of crystalline **24** allowed assigning its absolute and relative configuration, by comparison with the published co-crystal structure of a related inhibitor bound to the kinase domain of Itk.[24] After oxidation with mCPBA, hydrogenation of the dibromosulfone **25** under standard conditions could be accomplished without epimerization at the benzylic position, and allowed unambiguous assignment of the chiral centers in all related products. The radiosynthesis of [$^3H_2$]-**23** was performed under equivalent conditions, using tritium gas.

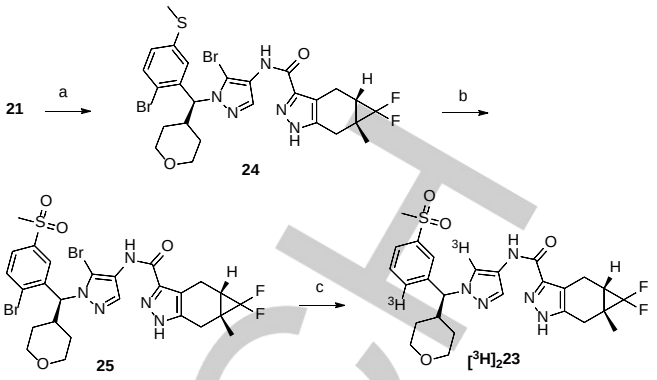

Scheme 7. Synthesis of [$^3H_2$]**23**. *Reagents and conditions*: a) Br_2, I_2, DCM, 0-25°C, 16 h; b) mCPBA, DCM, 0°C, 1h; c) $^3H_2$, Pd/C, DIEA, DMF, RT.

Lead selection and optimization

This section discusses the optimization of the leads selected after review of all structures available in the literature. After thorough characterization and identification of weaknesses as PET tracer candidates, those were primarily optimized to decrease non-specific binding, while aiming for optimal selectivity and pharmacokinetic properties.

1. Lead selection for ZAP70

The zeta-chain-associated protein kinase 70kDa (ZAP-70) is directly associated with the T cell receptor and is a central regulator of T cell activation, it has been an attractive medicinal chemistry target in immunology for many years.[26] Despite numerous efforts, no compounds has yet entered advanced clinical stages, mainly due to selectivity issues. Initial attempts to optimize the most promising inhibitors rapidly confirmed the challenge of improving their off-target profile. We did not identify suitable leads for developing T cell specific ligands, and did not pursue this target further.

2. Ligands for PKC θ

For the development of a PKC θ ligand as a T cell tracer, a review of the available chemical matters showed that compound **26**[21] (Figure 1) was the most selective inhibitor, and we focused on its optimization. This inhibitor has high affinity, reasonable selectivity but a high chromatography hydrophobicity index on immobilized artificial membranes[19,27] (CHI(IAM)), suggesting high non-specific binding (Table 2). Initial structure activity relationship indicated that the fluorine was required to provide the right torsion angle, and that the chlorine could be substituted by fluorine without loss of affinity. To reduce non-specific binding, the (*R*)-3-methyl-2-butyl-2-ol side-chain was converted into a 1,1,1-trifluoro-2-propyl-2-ol (**4**), decreasing the pKb value of the piperazine ring from 8.5 to 6.6 and the CHI(IAM) value from 61 to 39, with only a slight decrease in affinity for PKC θ. Selectivity versus LATS1, a serine/threonine-protein kinase encoded by the *LATS1* gene in humans, however decreased significantly and could not be recovered by further derivatization, leading to discontinuation of this series.

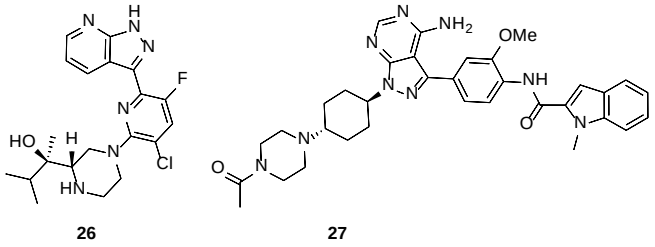

26 **27**

Figure 1. Structures of PKC θ inhibitor **26** and LCK inhibitor **27** selected as leads for optimization.

Table 2. Compound profiling

target	Cpd	IC_{50} [nM][a]	Selectivity [b]		CHI(IAM)	LSE [c]	MDCK[d]
PKC θ	**26**	0.1	30x	LATS1	61	5.6	3.9/2.0
	4	0.45	5x	LATS1	39	5.9	n.t.
Lck	**27**	0.2	2x	Hck	51	5.7	n.t.
	9	1	2x	Lyn	37	5.7	2.5/1.1

[a] IC_{50} measured by fluorescence using a mobility shift assay with a LC3000 Caliper Life Sciences system[34]; [b] Selectivity with regard to the second highest affinity target in panels of respectively 111, 24, 164 and 40 pharmacologically-relevant targets; [c] Ligand Specific Efficiency index[19], LSE = IC_{50}/log(CHI(IAM)); [d] Permeability as P_{app}x10^{-6} cm s^{-1} and efflux ratio in a Madin Darby Canine Kidney (MDCK) cell line transfected with the human multidrug resistance (MDR1) gene.

3. Ligands for Lck

As an additional option, we selected the Lck inhibitor A-770041 (**27**),[29] as starting point for tracer development. Compound **27** displays high affinity for Lck and reasonable selectivity. Despite an encouraging Ligand Specific Efficiency (LSE) index[19] of 5.7, its CHI(IAM) value of 51 is relatively high, and its clearance too slow for imaging ($t_{½}$= 3.2 h in Balb/c mouse). To address these issues, we explored the replacement of the acetylpiperazinyl-cyclohexyl moiety, and prepared a series of compounds inspired by the work published by Calderwood et al.[30] Ultimately, replacement by an isoxazolidine group (**9**) retained potency and improved non-specific binding significantly. Unfortunately, the target selectivity profile of **9**, while different from **27**, is not superior to the lead molecule (Table 2). The physicochemical properties of **9** also remain far from the range desirable for PET tracers, with a total polar surface area (tPSA) of 129 $Å^2$ and low permeability. We therefore concluded that this scaffold did not warrant further investigation and decided to focus on the last target, Itk.

4. Ligands for Itk

Among the four targets we selected initially, Itk displays the most pronounced T cell specific expression pattern. Several highly potent inhibitors with diverse chemical structures have been published, and to identify the best starting point for tracer optimization, we evaluated both the covalent (**28**)[31] and reversible inhibitors (**29**, **30**)[28,32] illustrated in Figure 2.

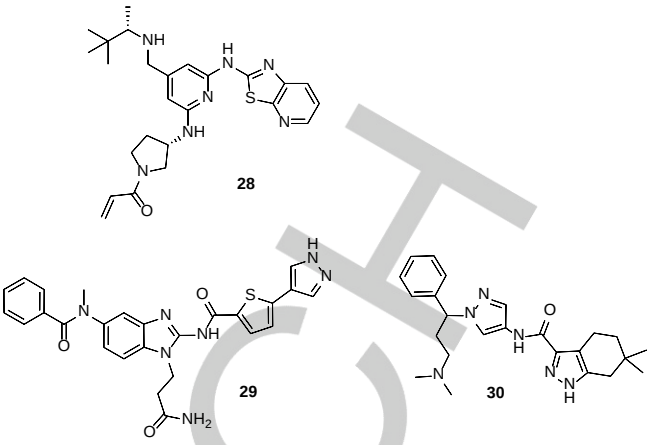

28 **29** **30**

Figure 2. Structures of covalent (**28**) and reversible (**29**, **30**) Itk inhibitors selected as leads for evaluation.

All three compounds were analyzed for potency, inhibition of key off-target kinases and potential for non-specific binding.

The covalent inhibitor **28** has a high affinity for Itk (Table 3), but we observed that it binds with similar potencies to the Cys-containing Tec family kinases (Itk, Tec, Bmx, Btk, Txk). Tec family members are widely expressed in the hematopoietic compartment, therefore strongly limiting the potential T cell specificity of **28**. We therefore deprioritized this compound for PET tracer optimization.

Table 3. Profile of selected Itk inhibitors.

Cpd	IC_{50} [nM]	Selectivity (fold)[a]	CHI(IAM)	LSE [b]	% HSA binding[c]	MDR1-MDCK[d]
15	10	8x IRAK1 3x MAP4K3	43	4.9	95.4	1.1/8.8
18	1.5	20x IRAK1 38x MAP4K3	46	4.8	94.9	0.7/6.1
22	0.8	22x IRAK1	30	6.2	85.7	0.9/11
23	0.3	20x IRAK1	32	6.4	89.2	0.5/6.5
28	0.8	1.5x Txk, Bmx 400x IRAK4	49	5.4	88.2	1.5/14
29	0.5	4x IRAK1 0.5x Flt3	29	6.4	93.6	1.0/2.8
30	31	12x IRAK1	59	4.2	93.2	1.0/11

[a] Selectivity with regard to the second highest affinity target in a panel of 24 related kinases; [b] Ligand Specific Efficiency index, LSE = pIC_{50}/log(CHI(IAM)); [c] binding to Human Serum Albumin binding; [d] Permeability as P_{app}x10^{-6} cm s^{-1} and efflux ratio in a Madin Darby Canine Kidney (MDCK) cell line transfected with the human multidrug resistance (MDR1) gene.

In contrast, reversible inhibitors proved selective with regard to Tec family members. While aminomethyl-benzimidazole **29** was remarkable for its biochemical potency, it demonstrated very little selectivity towards IRAK1/4 and Flt3. We thus focused on tetrahydroindazole **30**, which despite a lower affinity for Itk offered better kinome selectivity, and a better overall radioligand

property profile. In particular, we were encouraged by its lower MW and PSA, leading to a ligand efficiency[33] (LE = 0.33) comparable to the more potent, but heavier **29** (LE = 0.34).

The most critical property to be improved in compound **30** is its very high non-specific binding to cell membranes, illustrated by a CHI(IAM) value of 59. We hypothesized that this was largely influenced by its basic amine side-chain. Down-modulating the pKa of the tertiary amine by introducing a fluoroethyl substituent (**15**, Scheme 8) led to a substantial reduction of the CHI(IAM) value to 43, together with a 3-fold improvement in potency. Conveniently, the fluoroethyl side-chain represents an easy point for radiolabeling with ^{18}F, late in the synthesis of the tracer.

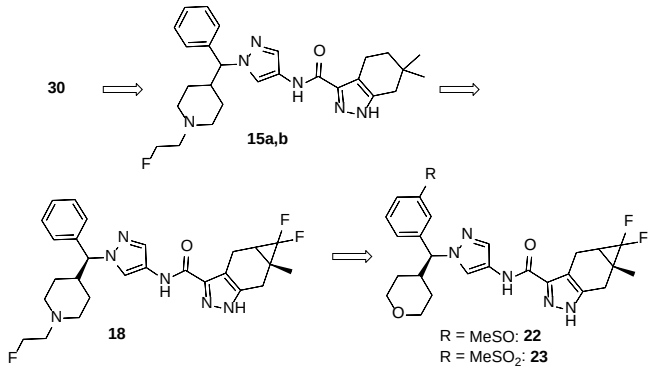

Scheme 8. Itk radioligand optimization of the tetrahydroindazole series

To better understand the potential of **15** as an imaging tracer, we investigated its pharmacokinetic parameters and tissue distribution (Table 4). The study was performed with a pharmacological i.v. dose of 1 mg/kg in rats. Unfortunately, compound **15** showed an unfavorable tissue distribution profile, suggesting high non-specific binding: Ten minutes after dosing, **15** had already strongly accumulated in the spleen, which is a critical target organ for the assessment of T cell imaging agents. This finding prompted us to attempt a more radical change in molecular properties, and we removed the basic group from the molecule, a known liability for unspecific binding.

Table 4. PK parameters and tissue distribution

Cpd	Cl[a]	Vss[b]	$t_{½}$ [h] [c]	Tissue/blood ratio after 10 min and 1 h		
15	60	4.5	1.1	spleen	4.8	10.1
22	33	1.1	0.5	spleen	0.4	-
				thymus	0.6	1.1
				muscle	0.8	1.1
23	34	3.5	1.3	spleen	0.5	0.4
				thymus	0.5	0.9
				muscle	0.8	0.6

[a] Cl: clearance, [mL.min^{-1}.kg^{-1}]; [b] Vss: distribution volume at steady state, [L.kg^{-1}]; [c] terminal half-life.

It had been previously demonstrated that a further improvement in potency and selectivity can be achieved with the fusion of a difluorocyclopropyl group to the tetrahydroindazole moiety.[24] This was applied to **15**, leading to a more potent molecule (**18**) with an IC_{50} of 1.5 nM. Compound **18** has an almost unchanged LSE index despite added hydrophobicity.

We then replaced the fluoroethyl-piperidine side-chain by a tetrahydropyrane, compensating the loss of polarity by placing a methylsulfoxide on the benzene ring, which adds a strong dipole in the hydrophobic region, while maintaining the difluorocyclopropyl group successfully introduced in compound **18**. This led to compound **22**. Indeed, while these modifications retained potency and selectivity, they also decreased non-specific binding dramatically, with a CHI(IAM) value dropping from 46 to 30. *In vivo*, this translated into a much more favorable tissue distribution in spleen, thymus and muscle, with a blood/organ concentration ratio now close to unity and a distribution volume reduced to 1.1 L/kg. The observed elimination half-life of 0.5 h is within an acceptable range for ^{18}F PET ligands.

Interestingly, the *in vitro* metabolite profile of **22** in rat liver microsomes (data not shown) indicated rapid oxidation to the corresponding sulfone **23**. This led us to re-analyze the samples of the pharmacokinetic study conducted with **23**, confirming that this transformation was also taking place *in vivo*, and showing that **23** actually constitutes a major circulating metabolite one hour after injection of **22** (Figure 3).

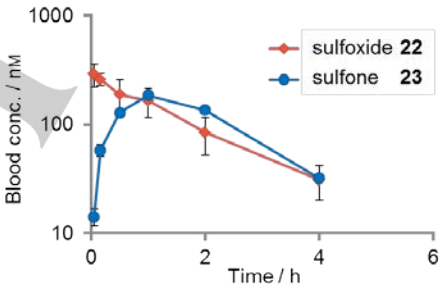

Figure 3. Pharmacokinetic profile of sulfoxide **22** and of its sulfone metabolite **23** after i.v. dosing in rats.

Luckily, compound **23** turned out to be 3-fold more potent than its parent **22**, more than compensating for a slight increase in non-specific binding. Compound **23** has the best LSE value in the series (6.4). As the pharmacokinetic profile and tissue distribution of **22** and **23** proved similar, we selected **23** for further validation of Itk as a target for T cell imaging.

In vivo profiling

While the preliminary selection of Itk as a target for T cell imaging was primarily based on published RNA expression data on relevant cell types and tissue distribution, the optimization of potency and selectivity of the ligand itself relied on biochemical kinase inhibition assays. These assays are individually tuned for robustness and sensitivity, allowing an efficient profiling process. They however do not allow a precise comparison of affinities across kinases, and poorly predict the potential effect of binding to off-target kinases in imaging applications. The influence of off-target affinities is highly dependent on expression level and kinase activation states in target tissues. Therefore, while the *in vitro* selectivity profile of the Itk-inhibitors was a valuable guide in the ligand optimization process, a meaningful assessment of T

cell specificity and sensitivity can only be achieved using *in vitro* tissue binding studies with radiolabeled compounds.

Overall, compound **23** had the desired profile for a proof of concept study using tritium labeling. To achieve high specific activity, two bromine atoms were introduced at the phenyl and the pyrazole ring of **21** (Scheme 7, compound **24**), allowing the introduction of two tritium atoms by reductive displacement. The resulting [^{3}H]$_2$-**23** had sufficient specific activity (27.0 Ci/mmol) to assess the feasibility of imaging T cells *in vitro* and *in vivo*.

Our first objective was to demonstrate that [^{3}H]$_2$-**23** leads to a displaceable, selective *in vitro* radiolabeling of T cell rich tissues of human and murine origin. Indeed**,** autoradiography of sections of human pharyngeal tonsils and mouse inguinal lymph nodes, incubated with 10 nM [^{3}H]$_2$-**23,** showed a strong labeling of the lymphatic tissue from both species. The autoradiographic resolution achieved with human tonsils allows the assignment of specific labeling to the lymphatic tissue, while sparing the tonsillar epithelium and crypts (Figure 4b). Specificity of labeling could be demonstrated by blocking the signal with an excess of cold **23**, as well as with the structurally unrelated Itk-inhibitor **28.** In slices where [^{3}H]$_2$-**23** binding is blocked with unlabeled Itk inhibitors (Figure 4c,d) the residual radioactivity is uniformly distributed indicating a low level of unspecific binding.

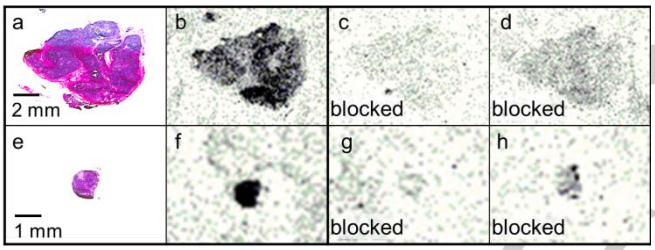

Figure 4. *In vitro* autoradiography of human pharyngeal tonsils (serial sections a-d) and mouse inguinal lymph nodes (sections e-h) showing specific binding of radiolabeled Itk inhibitor **[^{3}H$_2$]-23** to T cell rich tissue in both species; (a, e) hematoxylin-eosin stain; (b, f) incubation with 10 nM **[^{3}H$_2$]-23**; (c, d, g, h) incubation with 10 nM **[^{3}H$_2$]-23** in the presence of 10 µM unlabelled **23**; (c, g) or in the presence of 10 µM of a structurally unrelated Itk inhibitor (d, h), **28.**

A key parameter for *in vivo* PET tracer imaging is rapid tissue distribution combined with rapid elimination of the radioactive probe, matching the half-live of the radioisotope, without the formation of interfering radio-metabolites. To prove the suitability of the tetrahydro-indazole class of Itk-inhibitors as a lead for further [^{18}F] PET tracer optimization, we evaluated the ability of [^{3}H$_2$]-**23** to label T cells in an *in vivo* experiment, one hour after i.v. dosing in male C57/BL6 mice. The T cell specificity of the signal was confirmed by comparing labeling intensity in T cell rich organs in naïve and partially T cell depleted (anti-CD4 treated) animals, using quantitative whole body autoradiography (QWBA, Figure 5). Special focus was put on the signal distribution in lymphatic organs such as thymus, spleen and lymph nodes. Visual inspection of the autoradiographic images does not show a strong contrast between tissues, and interpretation is facilitated by the quantification of the radioactivity signal (Table 5). Nevertheless, a clear punctuated pattern of radioactivity can be observed in the sagittal sections of the spleen, which is consistent with labeling of the T cell rich regions in the white pulp of this organ. The radioactive signal also decreases in the lymph nodes after T cell depletion. Overall, a broad and fast tissue distribution of [^{3}H$_2$]-**23** related radioactivity was observed one hour post dose. Measurable concentrations were detected in 53 out of 55 tissues and were generally low, reflecting a high systemic clearance rate. Table 5 lists the tissue concentration of total radiolabeled components in representative tissues, including spleen and lymph nodes.

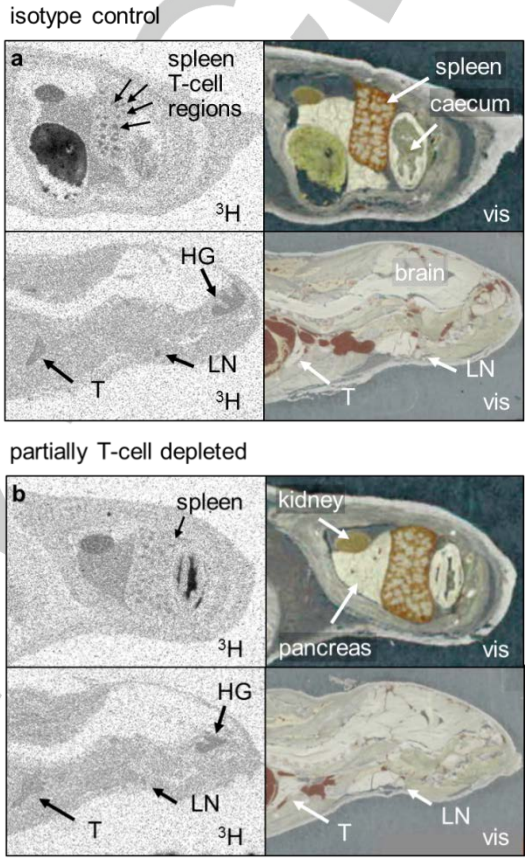

Figure 5. Autoradiographs (^{3}H) and visual scans (vis) of the spleen region in sagittal whole body sections from mice (1 h after a single intravenous nominal 25 µg/kg [^{3}H$_2$]-**23** dose. Slices used for autoradiography are 40 µM thick, dehydrated, and the darkest areas in the autoradiographs correspond to the highest concentration of radioactivity. a) naïve mouse (isotype control mAb pre-treated), upper panel: abdominal region with punctuated pattern of radioactivity in the white pulp of the spleen consistent with labeling of the T cell rich areas, lower panel: head and neck region with increased radioactivity in the thymus (T), submandibular lymph nodes (LN) and the harderian gland (HG); b) partially T cell depleted mouse (anti CD4 mAb pre-treated): reduced signal in the T cell areas of the spleen and the submandibular lymph nodes, no change in the harderian gland, thymus and background signal.

Levels above 10 pmol/g in isotype control pre-treated mice were only observed in the liver (164 pmol/g), and other excretory or secretory organs like kidney (11.6 pmol/g) and various glands (e.g. harderian gland 10.3 pmol/g), which is a common finding for many low molecular weight radioligands. Labeling of lymphoid tissue (thymus, white pulp of spleen, submandibular lymph nodes) was in the range 4.47 to 7.03 pmol/g.

Table 5. Tissue concentration of total radiolabelled components [pmol/g] in main organs, 1 h after an i.v. dose of 25.0 µg/kg [^{3}H]23 to male control and T cell depleted mice.

Tissue	Control[a]	T cell depleted[b]
Brain	0.181	0.131
Fat (white)	1.12	1.37
Heart	2.70	2.85
Lung	3.42	3.56
Lymph nodes (submandibular)	7.03	4.14
Muscle	2.50	2.63
Pancreas	4.97	5.06
Spleen (red pulp)	2.58	2.37
Spleen (T cell rich region, white pulp)	7.63	5.21
Thymus	6.97	7.03

[a] Control animals pre-treated with isotype control antibody. [b] Animals treated with T cell depleting antibody.

The extent of T cell depletion in lymphoid tissues was independently quantified in an identically depleted satellite group by FACS counting of T cells in spleen and lymph nodes (Figure 6).

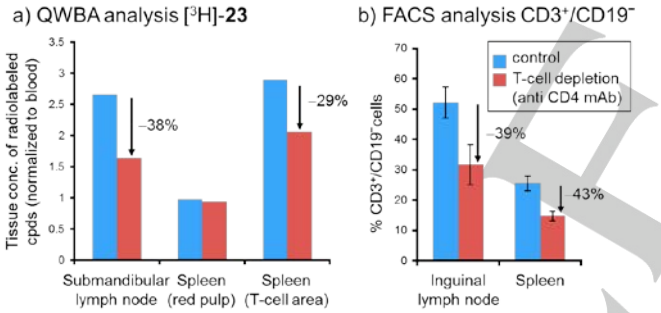

Figure 6. a) Tissue distribution of **[^{3}H$_2$]-23** related radioactivity (blood normalized) at 1 h post-dose in QWBA experiment in a naïve and a partially T cell depleted mouse (single experiment: no error bars). b) T cell depletion measured by FACS analysis of T cell content (% CD3$^+$/CD19$^-$ of total lymphocytes) in inguinal lymph node and spleen (satellite groups, n=6, combined data from 26 h and 30 h after mAb injection, control group treated with an isotype matched control mAb).

Comparing blood-normalized tissue concentrations of total radiolabeled components in lymphatic tissue of control mice with those of partially T cell depleted mice, a signal reduction of 38% and 29% was observed in submandibular lymph nodes and in the T cell rich regions (white pulp) of the spleen, respectively (Figures 5 and 6a). This result matches the T cell depletion values of 39% and 43% obtained by FACS analysis of lymph nodes and spleen in identically treated satellite animals (Figure 6b). In contrast, only 4% decrease of radioactive signal was observed in the T cell poor region of the spleen (red pulp). Although measured radioactivity does not differentiate between [^{3}H$_2$]-**23** and potential metabolites, the observed decrease in signal in the immune compartments indicates that this tracer indeed detects the reduction in T cell numbers in partially T cell depleted mice. There was almost no signal change in the thymus (+5%), paralleling observations made with CD4 and CD8 targeting agents, which also did not show T cell reduction in the thymus after anti-CD4 mAb treatment.[13] This is likely due to a non-saturating dose of GK1.5 antibody, combined with a partial blood-thymus barrier.

Conclusions

In this study we have evaluated four potential target proteins for a pan T cell specific PET tracer. Combining the mRNA expression data of the potential targets with the selectivity profile and physico-chemical properties of available ligands led to the identification of the T cell specific kinase Itk as the most promising candidate. Itk inhibitors of the tetrahydro-indazole class could be optimized to sub-nanomolar binding affinities with favorable parameters for binding specificity and pharmacokinetic parameters. Specificity of the probe was shown by *in vitro* autoradiography of human tonsils and mouse lymph nodes using tritiated [^{3}H$_2$]-**23**, confirming selective and displaceable labelling in lymphatic tissue. Finally, *in vivo* studies and QWBA in control and partially T cell-depleted mice demonstrated a reduction of radioactive signal in the T cell rich regions of the spleen and in lymph nodes, one hour after dosing of [^{3}H$_2$]-**23**. This matches the values of T cell depletion determined by flow cytometry.

While being a useful tool for target validation, **23** does not yet have the optimal profile required for a PET tracer. Its pharmacokinetic half-life is too long for [^{18}F] PET imaging. Using current methodology, the difluoro-cyclopropyl group already present in the molecule is not suited for introduction of [^{18}F] with sufficient specific activity, due to isotopic dilution. Other features which still need improvement are its low permeation and Pgp-mediated efflux, which would be prohibitive for imaging T cells in the CNS compartment.
This work nevertheless demonstrates that imaging T cells *in vivo* is feasible and that Itk-selective radiotracers have the potential to be used for PET imaging in the clinic.

Experimental Section

Biology

Autoradiography

Human tonsils were obtained from two patients following tonsillectomy. The study was conducted in accordance with the ethical principles originating in the Declaration of Helsinki and approved by the local Ethics Committee (study PJMR1000244). All subjects provided written informed consent before participating in the study. Eight week old male C57BL/6 mice were commercially purchased (Harlan, Itingen, Switzerland) and and inguinal lymph nodes were removed following termination. The study was conducted in accordance with Swiss federal law for animal protection and approved by the Veterinary Office of the Canton Basel-Stadt.

Frozen sections were cut 20 um thick with a microtome-cryostat and thaw-mounted on poly-*L*-lysine coated microscope slides and stored at

−80°C. Before incubation with labelled ligand, the sections were dried under a stream of cold air. Target binding autoradiography was performed according to the following procedure: after 20 min pre-incubation at RT in Krebs Tris buffer, the sections were incubated for 2 h at RT in the same buffer (20 mM Tris pH 7.4, 118 mM NaCl, 5.6 mM glucose. 1.2 mM KH_2PO_4, 4.78 mM KCl, 1.8 mM $CaCl_2$, 1.2 mM $MgSO_4$) supplemented with 10 nM [$^3H_2$]**-23** (27 Ci/mmol) with and without the competitor. After incubation, the slides were briefly dipped in ice cold distilled water followed by two 10 min washes in ice-cold buffer and brief dipping in ice-cold distilled water to remove salts. The sections were dried under a stream of cold air. Autoradiograms were generated by exposing the labelled tissue to a Tritium Phosphor screen medium (7001489 TR) at RT for 24 h. Data from binding were analysed with the OptiQuant software of the phosphor-imager cyclone plus.

Animal pre-treatment: Eight week old male C57BL/6 mice (Harlan, Itingen, Switzerland) were randomized to isotype control (rat IgG2b, BioLegend, USA) or anti-CD4 depleting antibody (clone GK1.5, BioLegend, USA) treatment groups. Animals received a single 1mg intravenous injection to induce partial T-cell depletion. Satellite groups subsequently continued into parallel QWBA or flow cytometry analysis readouts.

Animal dosing: The vehicle used for intravenous bolus administration of [^{3}H]**23** was an ethanol/0.9% saline solution (5/95, w/w). Mice were dosed with a single intravenous tracer dose of nominal 25 μg/kg [^{3}H]**23** (50 MBq/kg) 24 h after antibody pre-treatment.

QWBA (Quantitative Whole Body Autoradiography): In brief, mice (n = 1 per time point) were sacrificed one hour post [^{3}H]-**23** dosing, after deep anaesthesia (3-5% isoflurane, 95-97% O_2). The carcasses were deep-frozen by transfer into a heptane/dry ice mixture, where they were kept at −70°C for approximately 15-30 min. The carcasses were then stored in a deep-freezer below −20°C for at least 24 h; thereafter, they were rapidly shaved and stored again below −20°C; all subsequent procedures were performed at temperatures below −20°C to minimize diffusion of radiolabeled material in the tissues. Blood samples were collected from the sublingual vein of each mouse before freezing, for quality control purposes. In these samples, radioactivity was determined by liquid scintillation counting. The frozen carcasses were embedded in a mold on a microtome stage by adding an ice-cold aq. solution of 2% low viscosity sodium carboxymethylcellulose; the embedding block was frozen for approx. 45 min in a heptane/dry ice mixture at −70°C followed by a temperature stabilization overnight in a −20°C freezer. The animals were sectioned in the sagittal plane using a CM3600 cryomicrotome (Leica Microsystems GmbH, D-Nussloch) according to the method of Ullberg,[35] using disposable blades (Feather Inc.). Several lengthwise 40 μm sections were taken at varying depths; based on sectioning of the requisite organs, tissues and body fluids. A block of [^{3}H] radiolabeled standards, containing 9 standards prepared in blood and assayed by liquid scintillation counting, was sectioned in the same manner and on the same day as the mice were sectioned. The sections were dehydrated in the cryomicrotome at −23°C for at least 48 h and placed under controlled light conditions in direct and close contact with Fuji BAS MS2025 imaging plates (Fuji Photo FilmCo., Ltd., J-Tokyo, provided by GE Healthcare) for 7 d at RT in a lead shielding box. After exposure, the plates used for [^{3}H]autoradiography were transferred into a Fuji BAS 5000 TR phosphorimager (Fuji Photo Film Co., Ltd., J-Tokyo) and scanned with 50 μm scanning steps to produce an autoradiogram. Concentrations of total radiolabeled components in tissues/matrices were determined by comparative densitometry and digital analysis of the autoradiograms using an MCID/Analysis image analyzer (Imaging Research, St. Catharines, Ontario, Canada)

Flow cytometry Mice were sacrificed 25 hours post anti-CD4 antibody treatment and single cell suspensions generated from lymph nodes and spleen tissues via 70μm sieves (Becton Dickinson, USA). Lymphocytes were isolated from whole blood using red blood cell RBC lysis buffer (eBioscience, USA). Cells were washed in fluorescence-activated cell sorting FACS buffer (PBS containing 2% bovine serum albumin BSA, 5mM ethylenediaminetetraacetic acid), blocked with anti-mouse CD16/CD32 antibody (Biolegend, USA). Lymphocytes were stained with CD3 (clone 145-2C11), CD4 (clone RM4-5), CD19 (clone 6D5) and CD8 (clone 53-6.7) fluorochrome-conjugated antibodies 30 min at 4°C. Washed and resuspended cells were acquired on a Fortessa flow cytometer (Becton Dickinson, USA). Data were analysed using the FlowJo software (Flow Jo LLC, USA).

Chemistry

General methods: ^{1}H NMR spectra were acquired on a Varian 400 MHz. Chemical shifts (δ) values are given in parts per million (ppm) relative to the residual solvent peak. Analytical LCMS conditions (%: percent per volume), column: Phenomenex Synergi® MAX-RP, 4x20 mm, 2.5 μm, 40°C, solvent A: water + 0.1% HCO_2H, solvent B: CH_3CN, gradient: 5% B for 0.5 min + from 5% to 95% B over 0.5 min + 95% B for 0.5 min + from 95% to 5% over 0.5 min + 5% B for 1 min; Flow : 2.0 mL/min

1,1,1-Trifluoro-2-(pyrazin-2-yl)propan-2-ol (1): A suspension of acetyl pyrazine (1.0 g, 8.2 mmol), trimethyl(trifluoromethyl)silane (1.7 g, 12.3 mmol) and K_2CO_3 (1.7 g, 12.3 mmol) in DMF (10 mL) was stirred at RT for 12 h. The reaction mixture was extracted with EtOAc and the combined organic layers were washed with water, dried using sodium sulfate, filtered and concentrated. The residue was purified on silica gel by flash chromatography (hexane/EtOAc, gradient: 100:0 to 85:15) to afford the desired product (0.9 g, 60%) as yellow oil: ^{1}H NMR (400 MHz, $CDCl_3$): δ 1.81 (s, 3 H), 5.48 (bs, 1 H), 8.59-8.61 (m, 1 H), 8.69 (d, *J* = 2.4 Hz, 1 H), 8.89 (s, 1 H).

1,1,1-Trifluoro-2-(piperazin-2-yl)propan-2-ol (2): Platinum(IV) oxide (250 mg) was added to a suspension of 1,1,1-trifluoro-2-(pyrazin-2-yl)propan-2-ol (500 mg, 2.6 mmol) in MeOH (15 mL). The resulting mixture was stirred under hydrogen (4 bar) for 24 h at RT, cooled to RT, and filtered through celite. The celite cake was washed with MeOH and the filtrate concentrated. The crude product (450 mg) was used as such in the next step. LC–MS: t_R=0.11 min, m/z: 199.2 [M+H].

2-(4-(3,5-Difluoro-6-(1h-pyrazolo[3,4-b]pyridin-3-yl)pyridin-2-yl)piperazin-2-yl)-1,1,1-trifluoropropan-2-ol (4): A suspension of **2** (120 mg, 0.6 mmol), 3-(4-(tert-butyldimethylsilyl)-3,5,6-trifluoropyridin-2-yl)-1H-pyrazolo[3,4-b]pyridine[22] **3** (200 mg, 0.5 mmol) and Hünig's base in NMP (8 mL) was stirred for 2 h at 150°C. The reaction mixture was cooled to RT, diluted in EtOAc and washed with water. The organic layer was extracted, washed with brine, dried over $MgSO_4$, filtered and concentrated. The crude product was purified by preparative HPLC (column: Kinetec® EVO C_{18}, 21.2x150 mm, 5 μm, solvent A: MeOH+0.1%TFA, solvent B: CH_3CN, flow: 15mL/min, gradient: from 15% B to 25% B over 2 min + from 25% B to 55% B over 8 min) to afford 50 mg (21%, yellow solid) of the desired product as a racemic mixture. The residue was purified by chiral preparative HPLC (column: CHIRALPAK® IA, 10x250 mm, 5 μm, solvent A: hexane, solvent B: EtOH, flow: 8 mL/min, isocratic: A:B 60:40) to afford enantiomerically pure **4** (13 mg, yellow solid): : LC–MS: t_R=0.48 min, m/z: 429.3 [M+H]. ^{1}H NMR (300 MHz, CD_3OD): δ 1.98 (s, 3 H), 3.39-3.53 (m, 2 H), 3.63-3.67 (m, 1 H). 3.77-3.80 (m, 1 H), 3.92-3.96 (m, 1 H), 4.07-4.12 (m, 1 H), 4.33-4.38 (m, 1 H), 7.75 (dd, *J* = 4.8 Hz, 4.8 Hz, 1 H), 7.95 (dd, *J* = 8.1 Hz, 8.1 Hz, 1 H), 9.02 (m, 1 H), 9.26 (dd, *J* = 8.1 Hz, 1.5 Hz, 1 H).

Methyl 2-(4-(4-amino-3-iodo-1H-pyrazolo[3,4-d]pyrimidin-1-yl)isoxazolidine-2-carbonyl)benzoate (6): Methyl 2-(4-((methylsulfonyl)oxy)-isoxazolidine-2-carbonyl)benzoate[23] (760 mg, 0.7 mmol), 3-iodo-1H-pyrazolo[3,4-d]pyridine-4-amine (500 mg, 1.9 mmol) and K_2CO_3 (668 mg, 1.5 mmol) were dissolved in DMF (10 mL) at 0°C. The resulting suspension was heated to 90°C for 16 h. Water was added and the reaction mixture was extracted with EtOAc. The organic layers were washed with brine, dried with anhyd. Na_2SO_4, filtered and concentrated

under reduced pressure to give crude **6**, which was used in the next step without further purification. LC–MS: t_R=1.37 min, m/z: 494.95 [M+H].

3-Iodo-1-(isoxazolidin-4-yl)-1H-pyrazolo[3,4-d]pyrimidin-4-amine: Compound **6** (500 mg, crude) was dissolved in 10 mL of 4M HCl in dioxane at 0°C. The resulting suspension was stirred at 100°C for 16 h. The reaction mixture was treated with sat. aq. $NaHCO_3$ until pH=8 and EtOAc was added. The layers were separated and the organic extract was washed with brine, dried over anhyd. Na_2SO_4, and concentrated to afford the crude title product which was further used without purification. LC–MS: t_R=0.587 min, m/z: 332.85 [M+H].

tert-Butyl 4-(4-amino-3-iodo-1H-pyrazolo[3,4-d]pyrimidin-1-yl)isoxazolidine-2-carboxylate (7): 3-Iodo-1-(isoxazolidin-4-yl)-1H-pyrazolo[3,4-d]pyrimidin-4-amine (300 mg, 0.9 mmol) was dissolved in CH_2Cl_2 (30 mL) and Boc anhydride (236 mg, 1.1 mmol) and NEt_3 (228 mg, 2.2 mmol) were added at 0°C under a nitrogen atmosphere. The suspension was stirred at RT for 16 h. The reaction mixture was diluted with EtOAc and water, and the layers were separated. The organic layer was washed with brine, dried over anhyd. Na_2SO_4 and concentrated to afford the crude product which was purified by flash chromatography on silica gel (eluent: hexane to hexane/EtOAc 1:1) to give **7** as a white solid (150 mg, 38%). LC–MS: t_R=1.42 min, m/z: 432.90 [M+H]. ^{1}H NMR (300 MHz, DMSO-d_6): δ 1.44 (s, 9 H), 3.91-3.94 (m, 2 H), 4.1-4.3 (m, 2 H), 5.22-5.32 (m, 1 H), 8.2 (s, 1 H).

tert-Butyl 4-(4-amino-3-(3-methoxy-4-(1-methyl-1H-indole-2-carboxamido)phenyl)-1H-pyrazolo[3,4-d]pyrimidin-1-yl)isoxazolidine-2-carboxylate: Compound **7** (100 mg, 0.1 mmol), the boronate ester **8**[23] (141 mg, 0.2 mmol) and K_2CO_3 (80 mg, 0.3 mmol) were dissolved in DMSO (10 mL) and argon was bubbled through the suspension for 10 min. Pd(dppf)Cl_2 (19 mg, 0.01 mmol) was added and the degasification with argon was repeated. The reaction mixture was heated at 95°C for 1.2 h. After completion, the suspension was cooled to RT and water was added. The precipitate was isolated, washed with water and the filtrate extracted with EtOAc. The organic layers were washed with brine, dried over anhyd. Na_2SO_4 and concentrated to give the crude title product. LC–MS: t_R=1.58 min, m/z: 585.20 [M+H].

N-(4-(4-Amino-1-(isoxazolidin-4-yl)-1H-pyrazolo[3,4-d]pyrimidin-3-yl)-2-methoxyphenyl)-1-methyl-1H-indole-2-carboxamide (9): 80 mg crude *tert*-butyl 4-(4-amino-3-(3-methoxy-4-(1-methyl-1H-indole-2-carboxamido)-phenyl)-1H-pyrazolo[3,4-d]pyrimidin-1-yl)isoxazolidine-2-carboxylate were dissolved in 3 mL 4M HCl in dioxane at 0°C. The resulting suspension was stirred at RT for 16 h, then concentrated under reduced pressure. The crude product was purified by preparative HPLC (column: Zorbax C18, 21.2x150 mm, 5 μm, solvent A: water, solvent B: CH_3CN), flow: 20 mL/min, gradient: from 10% B to 20% B in 2 min then up to 80% B in 8 min) to afford **9** as a white solid (16 mg, 24%): LC-MS: t_R=1.44 min, m/z: 485.10 [M+H]. ^{1}H NMR (400 MHz, DMSO-d_6): δ 3.34-3.58 (m, 2 H), 3.95 (s, 3 H), 4.03 (s, 3 H), 4.08-4.12 (m, 2 H), 5.73-5.81 (m, 1 H), 7.12-7.16 (m, 1 H), 7.29-7.36 (m, 4 H), 7.58 (d, *J* = 8.4 Hz, 1 H), 7.69 (d, *J* = 8 Hz, 1 H), 8.11 (d, *J* = 8 Hz, 1 H), 8.27 (s, 1 H), 9.43 (s, 1 H).

Benzyl 4-benzoylpiperidine-1-carboxylate (32): Benzyl chloroformate (3.8 mL, 26.5 mmol) was added dropwise to a stirred solution of phenyl(piperidin-4-yl)methanone hydrochloride **10** (5 g, 22.15 mmol) and K_2CO_3 (9.17 g, 66.45 mmol) in THF at 0 °C. The mixture was stirred under argon overnight at RT, then quenched with ice cold water and extracted with EtOAc. The combined organic layers were washed with brine, dried over anhyd. Na_2SO_4 and concentrated under reduced pressure to give **32** (7 g, 97.76%); ^{1}H NMR (300 MHz, $CDCl_3$): δ 1.65-1.86 (m, 4 H), 2.92-3.08 (m, 2 H), 3.39-3.5 (m, 1 H), 4.2-4.3 (m, 2 H), 5.2 (s, 2 H), 7.3-7.4 (m, 5 H), 7.45-7.51 (m, 2 H), 7.55-7.61 (m, 1 H), 7.92-7.96 (m, 2 H).

Benzyl 4-(hydroxy(phenyl)methyl)piperidine-1-carboxylate (33): Sodium borohydride (2.46 g, 64.92 mmol) was added in portions to a stirred solution of compound **32** (7 g, 21.6 mmol) in MeOH (70 mL) under argon at 0 °C. The reaction mixture was stirred at RT overnight, quenched on ice and extracted with EtOAc. The combined organic layers were washed with brine, dried over anhyd. Na_2SO_4 and concentrated under reduced pressure to give **33** (7 g, quantitative). LC–MS: t_R=1.55 min, m/z: 326.0 [M+H].

Benzyl 4-(chloro(phenyl)methyl)piperidine-1-carboxylate (34): Thionyl chloride (3.12 mL, 43.05 mmol) was added dropwise to a stirred solution of **33** (7 g, 21.527 mmol) in CH_2Cl_2 (100 mL) under argon. The reaction mixture was stirred overnight at RT, excess solvent removed under reduced pressure. The residue was dissolved in CH_2Cl_2 and washed with water and brine. The organic layer was dried over anhyd. Na_2SO_4 and concentrated under reduced pressure to give **34** (7 g, 94.6%). LC–MS: t_R=1.69 min, m/z: 344.2 [M+H] which was directly used in the next step.

Benzyl 4-((4-nitro-1H-pyrazol-1-yl)(phenyl)methyl)piperidine-1-carboxylate (35): 4-Nitro-1H-pyrazole (1 g, 8.72 mmol) was added to a stirred mixture of **34** (3 g, 8.72 mmol), K_2CO_3 (2.4 g, 17.44 mmol) and KI (2.85 g, 17.44 mmol) in DMF under argon. The resulting reaction mixture was heated at 100 °C overnight, cooled to RT, quenched with ice and extracted with EtOAc. The combined organic layer was washed with brine, dried over anhyd. Na_2SO_4 and concentrated *in vacuo*. The residue was purified by column chromatography (60-120 mesh silica, solvent: EtOAc/hexane 1:1) to give yellow solid **35** (1.25 g, 34%). LC–MS: t_R=1.65 min, m/z: 421.05 [M+H]. ^{1}H NMR (300 MHz, $CDCl_3$): δ 1.1-1.43 (m, 4 H), 2.6-2.9 (m, 2 H), 4.1-4.16 (m, 2 H), 4.77 (d, *J* = 10.8 Hz, 1 H), 5.12 (s, 2 H), 5.31 (s, 1 H), 7.27-7.45 (m, 10 H), 8.11 (s, 1 H), 8.17 (s, 1 H).

Benzyl 4-((4-amino-1H-pyrazol-1-yl)(phenyl)methyl)piperidine-1-carboxylate (11): Zn powder (1.63 g, 29.73 mmol) was added to a stirred mixture of **35** (2.5 g, 5.95 mmol) and NH_4Cl (1.93 g; 29.73 mmol) in THF : water (2:1, 30 mL) at 0°C. The resulting reaction mixture was stirred overnight at RT. and then filtered through celite. The filtrate obtained was diluted with water and extracted using EtOAc (3 x 30 ml). The combined organic layers were washed with brine, dried over anhyd. Na_2SO_4 and concentrated under reduced pressure to give crude **11** (2.3 g, quantitative) as red gum. LC–MS: tR=1.366 min, m/z: 391.55 [M+H].

6,6-Dimethyl-1-(tetrahydro-2*H*-pyran-2-yl)-4,5,6,7-tetrahydro-1*H*-indazole-3-carboxylic acid (12): To a stirred solution of 6,6-dimethyl-4,5,6,7-tetrahydro-1*H*-indazole-3-carboxylic acid[28] (2 g, 9 mmol) in toluene (20 mL) was added 3,4-dihydro-2*H*-pyran (0.83 g, 9.9 mmol) and TFA (0.1 mL). The resulting reaction mixture was refluxed for 4 h and then diluted with AcOEt. The organic layer was washed with Na_2CO_3 solution, dried over anhyd. Na_2SO_4 and concentrated *in vacuo*. The crude compound purified by chromatography (60-120 mesh silica, 10% AcOEt in hexane as eluent) to obtain the protected intermediate (2.05 g, 74.3%) which was directly subjected to hydrolysis. The compound was dissolved in THF/MeOH/water (1:1:1, 45 mL) and LiOH.H_2O was added (2.61 g, 65.3 mmol). The resulting reaction mixture was stirred at room temperature for 4 h. The excess solvents were removed *in vacuo*, the remaining aqueous phase was acidified using aq. citric acid solution. The compound was extracted with AcOEt, the organic layer was dried over anhyd. Na_2SO_4 and concentrated under reduced pressure to get pale solid **12** (1.6 g, 88%). LC–MS: tR= 1.389 min, m/z: 279.3 [M+H]; 1H NMR (300 MHz, DMSO-d_6): δ 0.91 (s, 3 H), 0.93 (s, 3 H), 1.48-1.63 (m, 4 H), 1.65-1.70 (m, 1 H), 1.93-1.98 (m, 2 H), 2.11-2.32 (m, 1 H), 2.40 (s, 2 H), 2.56-2.72 (m, 2 H), 3.55-3.65 (m, 1 H), 3.81-3.90 (m, 1 H), 5.39 (dd, J = 2.7 Hz, 2.4 Hz, 1 H), 12.3 (bs, 1 H).

Benzyl 4-((4-(6,6-dimethyl-1-(tetrahydro-2H-pyran-2-yl)-4,5,6,7-tetrahydro-1H-indazole-3-carboxamido)-1H-pyrazol-1-yl)(phenyl)-methyl)piperidine-1-carboxylate ((±)-13): DIPEA (2.05 mL, 11.78 mmol) was added to a stirred solution of **12** (1.64 g, 5.89 mmol) and HATU (3.92 g, 11.78 mmol) in DMF (25 mL) at RT. The resulting reaction mixture was stirred for 10 min then **11** (2.3 g, 5.89 mmol) was added in portions. The reaction mixture was heated to 50 °C for 4 days, cooled to

0 °C and quenched with ice. The mixture was extracted with EtOAc and the combined organic layer was washed with water and brine, dried over anhyd. Na_2SO_4, filtered and concentrated *in vacuo.* The residue was purified using column chromatography (60-120 mesh silica, solvent: EtOAc/hexane 1:1) to obtain (±)-**13** (3.5 g, 65%). LC–MS: t_R=1.758 min, m/z: 651.25 [M+H].

6,6-Dimethyl-N-(1-(phenyl(piperidin-4-yl)methyl)-1H-pyrazol-4-yl)-1-(tetrahydro-2H-pyran-2-yl)-4,5,6,7-tetrahydro-1H-indazole-3-carboxamide ((±)-37): Pd-C (10%) (350 mg) was added to solution of **13** (3.5 g, 5.38 mmol) in MeOH (35 mL) and the mixture was stirred under H_2 atmosphere (balloon pressure) for 4 h. The mixture was filtered through celite and concentrated under reduced pressure to give crude (±)-37 (2.5 g, 90%) as brown solid. LC–MS: t_R = 1.39 min, m/z: 517.70 [M+H]. The compound was used in the next step without further purification.

6,6-Dimethyl-N-(1-(phenyl(piperidin-4-yl)methyl)-1H-pyrazol-4-yl)-4,5,6,7-tetrahydro-1H-indazole-3-carboxamide ((±)-14): Trifluoroacetic acid (1 mL) was added dropwise to a stirred solution of compound **(±)-37** (150 mg, 0.29 mmol) in CH_2Cl_2 (5 mL) at 0 °C and the mixture was then stirred at RT for 1 h. The excess solvent was removed under reduced pressure and the residue purified by prep HPLC (column: Phenomenex Gemini® NX-C_{18}, 19x150 mm, 5 µm, eluent A: 0.1% HCOOH in water, eluent B: CH_3CN, flow: 20 mL/min, gradient: 30% B for 2 min + from 30% B to 80% B over 8 min) to give (±)-**14** (12 mg, brown solid). LC–MS: t_R=0.328 min, m/z: 433.4 [M+H]. ^{1}H NMR (400 MHz, CD_3OD): δ 1.0 (s, 6 H), 1.15-1.42 (m, 6 H), 1.58-1.60 (m, 2 H), 2.50-2.65 (m, 6 H), 2.98-3.02 (m, 1 H), 7.28-7.30 (m, 1 H), 7.31-7.36 (m, 2 H), 7.48-7.50 (m, 2 H), 7.65 (m, 1 H), 8.12 (m, 1 H).

N-(1-((1-(2-Fluoroethyl)piperidin-4-yl)(phenyl)methyl)-1*H*-pyrazol-4-yl)-6,6-dimethyl-1-(tetrahydro-2*H*-pyran-2-yl)-4,5,6,7-tetrahydro-1*H*-indazole-3-carboxamide ((±)-38): Solid K_2CO_3 (156 mg, 1.16 mmol) was added to a solution of (±)-**37** (200 mg, 0.387 mmol) in DMF (5 mL) followed by 1-fluoro-2-iodoethane (101 mg, 0.58 mmol). The resulting reaction mixture was stirred overnight at RT, then diluted with water and extracted with EtOAc (3 x 10 mL). The combined organic layers were washed with brine, dried over anhyd. Na_2SO_4 and concentrated under reduced pressure to give compound (±)-**38** (100 mg, 45.9 %) which was directly used for the next step. LC–MS: t_R=1.27 min, m/z: 563.1 [M+H].

N-(1-((1-(2-Fluoroethyl)piperidin-4-yl)(phenyl)methyl)-1H-pyrazol-4-yl)-6,6-dimethyl-4,5,6,7-tetrahydro-1H-indazole-3-carboxamide (enantiomers 15a,b): HCl in dioxane (3 mL) was added to a solution of (±)-**38** (85 mg, 0.151 mmol), in dioxane (2 mL). The reaction mixture was stirred overnight at RT and excess solvent removed under reduced pressure to obtain (±)-**15** (50 mg, 69.15%). 40 mg of the racemic mixture were resolved using chiral prep. HPLC (column: Chiral Pak IA®,10x250 mm, 5µm, solvent A: n-hexane, solvent B: EtOH+0.1% DEA, flow: 6 mL/min, isocratic A:B 30:70) to obtain enantiomerically pure **15a** (first peak, 10.2 mg) and **15b** (second peak, 11 mg). Analytical data of (±)-**15**: LC–MS: t_R=1.35 min, m/z: 479.65 [M+H]. ^{1}H NMR (400 MHz, $CDCl_3$): δ 1.0 (s, 6 H), 1.35-1.50 (m, 3 H), 1.52-1.65 (m, 3 H), 2.0-2.1 (m, 2 H), 2.40-2.42 (m, 1 H), 2.6-2.8 (m, 6 H), 2.95-3.0 (m, 2 H), 4.45-4.46 (m, 1 H), 4.60-4.61 (m, 1 H), 4.79-4.81 (d, J = 10.8 Hz, 1 H), 7.28-7.36 (m, 2 H), 7.43-7.45 (m, 2 H), 7.52 (s, 1 H), 8.22 (s, 1 H), 8.56 (bs, 1 H).

5,5-Difluoro-5a-methyl-1-(tetrahydro-2*H*-pyran-2-yl)-1,4,4a,5,5a,6-hexahydrocyclopropa[*f*]indazole-3-carboxylic acid ((±)-16): To a stirred solution of ethyl 5,5-difluoro-5a-methyl-1,4,4a,5,5a,6-hexahydrocyclo-propa[*f*]indazole-3-carboxylate[24] (0.5 g, 1.95 mmol) in toluene (10 mL) was added 3,4-dihydro-2*H*-pyran (0.328 g, 3.9 mmol) and TFA (0.018 g). The resulting reaction mixture was refluxed for 14 h and then diluted with EtOAc. The organic layer was washed with sat. aq. Na_2CO_3, dried over anhyd. Na_2SO_4 and concentrated under reduced pressure. The crude compound was purified by chromatography (60-120 mesh silica, 15% AcOEt in hexane) to obtain the protected intermediate (0.3 g, 45%) which was directly hydrolysed by dissolving the crude product in THF/methanol/water (1:1:1, 9 mL) and adding $LiOH.H_2O$ (0.184 g, 4.4 mmol). The resulting reaction mixture was stirred at RT for 14 h, excess solvents were removed under reduced pressure, and the aq. layer acidified with aq. citric acid. The compound was extracted with EtOAc, the organic layer dried over anhyd. Na_2SO_4, filtered and concentrated under reduced pressure to obtain crude (±)-**16** (0.25 g, 90.8%) as gummy solid. LC–MS: tR= 1.467 min, m/z: 313.05 [M+H]; 1H NMR (300 MHz, DMSO-d_6): δ 1.38 (s, 3 H), 1.56-1.70 (m, 2 H), 1.75-2.0 (m, 4 H), 2.08 (s, 2 H), 2.1-2.22 (m, 2 H), 2.78-2.82 (m, 1 H), 3.59-3.63 (m, 1 H), 3.80-3.90 (m, 1 H), 5.41 (dd, J = 2.6 Hz, 2.4 Hz, 1 H).

Benzyl 4-((4-(5,5-difluoro-5a-methyl-1-(tetrahydro-2*H*-pyran-2-yl)-1,4,4a,5,5a,6-hexahydrocyclopropa[*f*]indazole-3-carboxamido)-1*H*-pyrazol-1-yl)(phenyl)methyl)piperidine-1-carboxylate (diastereomeric mixture 39): BOP (595 mg, 1.345 mmol) was added to a solution of (±)-**16** (280 mg, 0.9 mmol) in DMF (3 mL) followed by DIPEA (0.312 mL, 1.8 mmol). The reaction mixture was stirred for 10 min and (±)-**11** (525 mg, 1.35 mmol) was added in portions. The reaction mixture was stirred at RT for 48 h, cooled to 0 °C, quenched using ice cold water and extracted with EtOAc. The combined organic layers were washed with brine, dried over anhyd. Na_2SO_4, filtered and concentrated under reduced pressure. The crude compound was purified by column chromatography (60-120 mesh silica, solvent: EtOAc/hexane 1:1) to give diastereomeric mixture **39** (280 mg, 46%). LC–MS: t_R=1.70 min, m/z: 685.3 [M+H].

5,5-Difluoro-5a-methyl-N-(1-(phenyl(piperidin-4-yl)methyl)-1H-pyrazol-4-yl)-1-(tetrahydro-2H-pyran-2-yl)-1,4,4a,5,5a,6-hexahydrocyclopropa[f]indazole-3-carboxamide (diastereomeric mixture 17): Pd-C (10%) (50 mg) was added to a stirred solution of **39** (270 mg, 0.394 mmol) in EtOH (5 mL) and the mixture was hydrogenated under balloon pressure of hydrogen for 6 h. The reaction mixture was filtered through celite and concentrated under reduced pressure to give the crude diastereomeric mixture **17** (190 mg, 88%) as brown solid. LC–MS: t_R=1.37 min, m/z: 551.25 [M+H].

5,5-Difluoro-N-(1-((1-(2-fluoroethyl)piperidin-4-yl)(phenyl)methyl)-1*H*-pyrazol-4-yl)-5a-methyl-1-(tetrahydro-2*H*-pyran-2-yl)-1,4,4a,5,5a,6-hexahydrocyclopropa[*f*]indazole-3-carboxamide (diastereomeric mixture 40): 1-Fluoro-2-iodoethane (0.053 mL, 0.654 mmol) was added to a mixture of 17 (180 mg, 0.327 mmol) and K_2CO_3 (90 mg, 0.654 mmol) in DMF (3 mL). The resulting reaction mixture was heated at 80 °C for 1 h, cooled to RT, diluted with water and extracted with EtOAc. The combined organic layers were washed with brine, dried over anhyd. Na_2SO_4 and concentrated under reduced pressure to give crude **40** (195 mg, quantitative) LC–MS: t_R=1.36 min, m/z: 597.3 [M+H] which was directly used in the next step.

5,5-difluoro-N-(1-((1-(2-fluoroethyl)piperidin-4-yl)(phenyl)methyl)-1*H*-pyrazol-4-yl)-5a-methyl-1,4,4a,5,5a,6-hexahydrocyclopropa[*f*]indazole-3-carboxamide (stereoisomers 18a-d): A solution of **40** (180 mg, 0.30 mmol) in dioxane/HCl (5 mL) was stirred over night at RT. The excess solvents was removed *in vacuo.* The crude product was further purified using prep HPLC (column: Phenomenex Kinetex® C_{18}, 21.5x250mm, 5.0µm, solvent A: water+0.02% TFA, solvent B: CH_3CN:MEOH 1:1, flow: 20 mL/min, gradient: from 50% B to 60% B over 2 min + from 60% B to 80% B over 8 min) to obtain **18** as a racemic mixture of diastereoisomers (80 mg, 51.61%). The four stereoisomers were separated using chiral prep HPLC (Chiral Pak® IA, 10x250 mm, 5 µm, solvent A: n-hexane, solvent B: 0.1% DEA in EtOH:i-PrOH 3:1, isocratic A:B 65:35) to get **18a** (first peak, 7.5 mg, 4.9%), **18b** (second peak, 7 mg, 4.6%), **18c** (third peak, 3 mg, 2%), **18d** (fourth peak, 5 mg,3.3%). LC–MS: t_R=1.33 min, m/z: 513.25 [M+H], no separation of diastereoisomers. ^{1}H NMR (mixture of stereoisomers, 400 MHz, $CDCl_3$): δ 1.2-1.4 (m, 4 H), 1.4 (s, 3 H), 1.99-2.09 (m, 3 H), 2.4-2.51 (m, 1 H), 2.61-2.63 (m, 1 H), 2.64-2.77 (m, 2 H), 2.92-3.0 (m, 2 H), 3.05-3.1 (m, 1 H), 3.1-3.22 (m, 1 H), 3.23-3.28 (m, 1 H), 4.47-4.49 (m, 1

H), 4.59-4.61 (m, 1 H), 4.76 (d, *J* = 11.2 Hz, 1 H), 7.27-7.34 (m, 3 H), 7.41-7.44 (m, 2 H), 7.50 (s, 1 H), 8.14 (s, 1 H), 8.51 (s, 1 H).

(3-(Methylthio)phenyl)(tetrahydro-2H-pyran-4-yl)methanol ((±)-41): n-BuLi (1.6 M in hexane, 24 mL) was added to a solution of (3-bromophenyl)(methyl)sulfane (7 g, 34.8 mmol) in anhyd. THF (70 mL) at −78°C followed by dropwise addition of tetrahydro-2H-pyran-4-carbaldehyde (3.97 g, 34.8 mmol). The reaction mixture was slowly brought to RT and allowed to stir for another 2 h. The reaction mixture was quenched using sat. aq. NH_4Cl at 0 °C, and extracted with EtOAc. The combined organic layers were washed with brine, dried over anhyd. $MgSO_4$, filtered and concentrated in vacuo. The residue was purified using column chromatography (60-120 mesh silica, solvent: EtOAc/hexane 3:7) to give (±)-**41** (6 g, 73.1%) as pale yellow liquid. ^{1}H NMR (300 MHz, $CDCl_3$): δ 1.1-1.3 (m, 4 H), 1.89-1.93 (m, 2 H), 2.5 (s, 3 H), 3.24-3.42 (m, 2 H), 3.74-4.05 (m, 2 H), 4.31-4.34 (m, 1 H), 7.04-7.08 (m, 1 H), 7.18-7.29 (m, 3 H).

4-(Chloro(3-(methylthio)phenyl)methyl)tetrahydro-2H-pyran ((±)-42): Thionyl chloride (2.2 mL, 30.2 mmol) was dropwise added to a solution of (±)-**41** (6 g, 25.2 mmol) in anhyd. CH_2Cl_2 (60 mL) and the resulting reaction mixture was stirred at RT for 2 h. Excess of solvents was removed under reduced pressure and the crude product was dissolved in CH_2Cl_2 and washed with water and brine. The organic layer dried over anhyd. Na_2SO_4 and concentrated under reduced pressure to get crude (±)-**42** as yellow oil (6.2 g, 96%) which was directly used for the next step. ^{1}H NMR (300 MHz, $CDCl_3$): δ 1.2-1.5 (m, 4 H), 2.02-2.12 (m, 1 H), 2.5 (s, 3 H), 3.23-3.43 (m, 2 H), 3.86-3.92 (m, 1 H), 4.04-4.13 (m, 1 H), 4.52 (d, *J* = 9 Hz, m 1 H), 7.08-7.12 (m, 1 H), 7.17-7.31 (m, 3 H).

1-((3-(Methylthio)phenyl)(tetrahydro-2H-pyran-4-yl)methyl)-4-nitro-1H-pyrazole ((±)-43): Solid K_2CO_3 (6.68 g, 48.4 mmol) and KI (4 g, 24.2 mmol) were added to a solution of 4-nitropyrazole (2.73 g, 24.2 mmol) in 60 mL anh. DMF followed by (±)-**42** (6.2 g, 24.2 mmol). The resulting reaction mixture was heated at 100 °C for 14 h. The reaction mixture was cooled to RT, quenched with ice water and extracted using EtOAc (3 x 50 mL). The combined organic layers were washed with water and brine, dried over anhyd. Na_2SO_4 and concentrated under reduced pressure to give crude product which was purified by silica gel chromatography (EtOAc/hexane 1:4) to yield (±)-**43** (4 g, 50%) as yellow oil. ^{1}H NMR (300 MHz, $CDCl_3$): δ 1.2-1.22 (m, 2 H), 1.62-1.68 (m, 2 H), 1.9-2.0 (m, 1 H), 3.07-3.15 (m, 2 H), 3.26-3.34 (m, 2 H), 4.25 (d, *J* = 10.8 Hz, 1 H), 6.4-6.53 (m, 3 H), 6.66 (s, 1 H), 7.37 (s, 1 H), 7.94 (s, 1 H).

1-((3-(Methylthio)phenyl)(tetrahydro-2H-pyran-4-yl)methyl)-1H-pyrazol-4-amine (enantiomers 19a,b): A saturated aqueous solution of NH_4Cl (10 mL) was added to a solution of (±)-**44** (4 g; 12 mmol) in THF (40 mL) followed by Zn dust (3.9 g, 60 mmol). The reaction mixture was stirred at RT for 3 h until TLC analysis indicated completion of the reaction. The reaction mixture was filtered through a celite bed and washed with EtOAc. The organic layer was separated, dried over anhyd. Na_2SO_4 and concentrated under reduced pressure to give crude product (±)-**19** which was further purified using reverse phase prep HPLC (column: Phenomenex Kinetex® C_{18}, 21.2x150mm, 5 µm, solvent A: water+0.05% TFA, solvent B: CH_3CN/MeOH 1:1, flow: 18mL/min, gradient: from 20% B to 30% B over 2 min + from 30% B to 70% B over 8 min) to afford 1.5 g brown solid (1.50 g) which was further resolved using chiral prep HPLC (Lux® Cellulose-4, 10x250 mm, 5 µm, solvent A: hexane, solvent B: 0.1% DEA in EtOH/MEOH/i-PrOH, 50:25:25, isocratic A:B 65:35) to afford the pale solids *(R)*-**19a** (peak 1, (*R*)-enantiomer, 550 mg, 15%) and *(S)*-**19b** (peak 2, (*S*)-enantiomer, 550 mg, 15%), respectively. LC–MS: t_R =0.6 min, m/z: 303.9 [M+H]. Assignment of the absolute configuration was based on the X-ray crystal structure of **25**, which was synthesized from *(S)*-**19b**.

(5a*R*)-5,5-Difluoro-5a-methyl-N-(1-((*S*)-(3-(methylthio)phenyl)(tetrahydro-2*H*-pyran-4-yl)methyl)-1*H*-pyrazol-4-yl)-1,4,4a,5,5a,6-hexahydrocyclopropa[*f*]indazole-3-carboxamide (21): Enantiomerically pure (4a*S*,5a*R*)-5,5-difluoro-5a-methyl-1,4,4a,5,5a,6-hexahydrocyclopropa[*f*]indazole-3-carboxylic acid was prepared by separating the corresponding ethyl ester[24] by chiral HPLC (column: ChiralPak® IA, 10x250 mm, 5 µm, solvent: isocratic hexane/isopropanol/methanol 80:10:10, flow: 20 ml/min, first eluting peak), and subsequent hydrolysis. BOP (0.581 g, 1.315 mmol) was added to a solution of the chiral acid (0.2 g, 0.876 mmol) in 3 mL anhyd. DMF followed by DIPEA (0.31 mL, 1.75 mmol). After 10 min a solution of **19a** (0.265 g, 0.876 mmol) in anhyd. DMF was added slowly. The reaction mixture was stirred at 50°C for 4 h. After cooling to RT, the mixture was quenched with ice water and extracted with EtOAc (3 x 20 mL). The combined organic layers were washed with water and brine, dried over anhyd. Na_2SO_4 and concentrated under reduced pressure to give crude **21** (250 mg, 28%) which was directly used for the next step. LC–MS: t_R=1.548 min, m/z: 514.20 [M+H].

(5aR)-5,5-Difluoro-5a-methyl-N-(1-((1S)-(3-(methylsulfinyl)phenyl)(tetrahydro-2H-pyran-4-yl)methyl)-1H-pyrazol-4-yl)-1,4,4a,5,5a,6-hexahydrocyclopropa[f]indazole-3-carboxamide (22a,b): A solution of **21** (150 mg, 0.292 mmol) in 6 M *t*-butyl hydroperoxide in decane (3 mL) was stirred at RT for 1 h. The excess of solvents was removed under reduced pressure to give a crude product which was purified by reverse phase prep. HPLC (column: Phenomenex LUNA® C_{18}, 21.2x250 mm, 5 µm, solvent A: water+0.1% TFA, Solvent B: CH_3CN, flow: 20mL/min, gradient: from35% B to 45% B over 2 min + from 45% B to 65% B over 8 min) to afford 60 mg of the crude product. The diastereoisomers were separated by chiral prep HPLC (column: ChiralPak® IA, 10x250 mm, 5 µm, solvent: hexane/i-PrOH isocratic 65:35, flow: 9 mL/min) to afford **22a** (peak 1, 28 mg, 18%) and **22b** (peak 2, 29 mg, 19%) as pale solids. LC–MS: t_R =1.42 min, m/z: 530.15 [M+H]. ^{1}H NMR (400 MHz, CD_3OD): δ 1.2-1.36 (m, 4 H), 1.37 (s, 3 H), 1.62-1.67 (m, 1 H), 2.78-2.80 (m, 4 H), 3.03-3.2 (m, 4 H), 3.3-3.45 (m, 2 H), 3.86-3.93 (m, 2 H), 5.08 (d, *J* = 10.8 Hz, 1 H), 7.55-7.58 (m, 1 H), 7.59-7.65 (m, 1 H), 7.68 (s, 1 H), 7.72-7.74 (m, 1 H), 7.89 (d, *J* = 4.4 Hz, 1 H), 8.14 (s, 1 H).

(5a*R*)-5,5-Difluoro-5a-methyl-N-(1-((*S*)-3-(methylsulfonyl)phenyl)(tetrahydro-2*H*-pyran-4-yl)methyl)-1*H*-pyrazol-4-yl)-1,4,4a,5,5a,6-hexahydrocyclopropa[*f*]indazole-3-carboxamide (23): *m*CPBA (67 mg, 0.39 mmol) was added to a solution of **21** (100 mg, 0.194 mmol) in anhyd. CH_2Cl_2 (3 mL) at 0 °C. The reaction mixture stirred at 0 °C for 1 h, then diluted with CH_2Cl_2 and quenched with sat. aq. $NaHCO_3$. The organic layer was separated, washed with brine, then dried over anhyd. Na_2SO_4 and concentrated under reduced pressure. The crude product was purified by reverse phase prep HPLC (column: Zorbax XDB® C_{18}, 21.2x150 mm, 5 µm, solvent A: water+0.1% TFA, solvent B: CH_3CN, flow: 18mL/min, gradient: from 30% B to 40% B over 2 min + from 40% B to 70% B over 8 min) to afford **23** (14.5 mg, 14%) as a white solid. LC–MS: t_R =1.46 min, m/z: 546.20 [M+H]. ^{1}H NMR (400 MHz, $CDCl_3$): δ 1.2-1.36 (m, 4 H), 1.4 (s, 3 H), 1.59-1.62 (m, 1 H), 2.7-2.78 (m, 2 H), 3.04 (s, 3 H), 3.05-3.2 (m, 2 H), 3.28-3.41 (m, 3 H), 3.89-3.96 (m, 2 H), 4.81 (d, *J* = 11.2 Hz, 1 H), 7.54-7.59 (m, 2 H), 7.77-7.82 (m, 1 H), 7.85-7.88 (m, 1 H), 8.04 (s, 1 H), 8.18 (s, 1 H), 8.59 (bs, 1 H).

(5a*R*)-N-(5-Bromo-1-((*S*)-(2-bromo-5-(methylthio)phenyl)(tetrahydro-2*H*-pyran-4-yl)methyl)-1*H*-pyrazol-4-yl)-5,5-difluoro-5a-methyl-1,4,4a,5,5a,6-hexahydrocyclopropa[*f*]indazole-3-carboxamide (24): A catalytic amount of I_2 was added to a solution of **21** (300 mg, 0.584 mmol) in anhyd. CH_2Cl_2 (10 mL) at 0 °C followed by dropwise addition of Br_2 (0.187 g, 1.16 mmol). The reaction mixture was stirred overnight at RT. Additional Br_2 (0.187, 1.16 mmol) was added and the reaction mixture was kept at RT for an additional 12 h. The reaction was quenched with aq. $Na_2S_2O_3$ and extracted with dichloromethane (3 x 10 mL). The combined organic layers were washed with brine, dried over anhyd. Na_2SO_4 and concentrated under reduced pressure. The crude product was purified by reverse phase prep HPLC (column: Phenomenex Gemini® NX-C_{18}, 21.2x150 mm, 5 µ, solvent A: water+0.1% formic acid, solvent B: CH_3CN, flow: 20mL/min, gradient: from 30% B to 40% B over

2 min + from 40% B to 80% B over 8 min) to afford **24** (50 mg, 13 %). LC–MS: t_R =1.681 min, m/z: 672.0 [M+H] which was directly used in the next step.

(5a*R*)-N-(5-bromo-1-((*S*)-(2-bromo-5-(methylsulfonyl)phenyl)(tetrahydro-2*H*-pyran-4-yl)methyl)-1*H*-pyrazol-4-yl)-5,5-difluoro-5a-methyl-1,4,4a,5,5a,6-hexahydrocyclopropa[*f*]indazole-3-carboxamide (25): *m*CPBA (25.7 mg, 0.15 mmol) was added to a solution of **24** (50 mg, 0.074 mmol) in anhyd. CH_2Cl_2 (3 mL) at 0 ^{0}C. The resulting reaction mixture was stirred at 0 ^{0}C for 1 h, diluted with CH_2Cl_2 and quenched with sat. aq. $NaHCO_3$. The organic layer was separated, washed with brine, dried over anhyd. Na_2SO_4 and concentrated under reduced pressure. The crude product was purified by reverse phase prep. HPLC (column: Waters XBridge® C_{18}, 21.2x150 mm, 5 µm, solvent A: water, solvent B: CH3CN, flow: 15mL/min, gradient: from 30% B to 40% B over 2 min + from 40% B to 90% B over 8 min), to afford **25** (22 mg, 43%) as colourless gum. LC–MS: t_R =1.53 min, m/z: 703.9 [M+H]. ^{1}H NMR (300 MHz, $CDCl_3$): δ 1.14-1.32 (m, 5 H), 1.4 (s, 3 H), 1.56-1.58 (m, 1 H), 2.72-2.78 (m, 2 H), 3.02 (s, 3 H), 3.06-3.38 (m, 5 H), 3.9-3.96 (m, 2 H), 5.79 (d, 1 H), 7.69-7.79 (m, 2 H), 8.26-8.28 (m, 2 H), 8.58 (d, *J* = 2.1 Hz, 1 H).

Method for the tritiation of 23.
Pd on activated charcoal (10%, 15 mg) was added to a solution of 2 mg **25** and 0.7 mg DIPEA in 2 ml anhyd. DMF. The mixture was treated with hydrogen at 1 atm at RT for 1.5 h under vigorous stirring and then filtered through celite. The filtrated was diluted with water and extracted with EtOAc. The organic layer was separated, washed with water, dried over anhyd. Na_2SO_4 and evaporated under reduced pressure to afford **23**. LC–MS: t_R = 3.70 min, m/z: 545.9 [M+H]. The product was analyzed on chiral column and eluted at the same t_R as the authentic sample. No epimerization could be detected.

Acknowledgements

The authors have the pleasure to acknowledge the support of Dr. Bernard Pirard for molecular modeling; Dr. Ina Dix for X-ray analysis; Emanuele Mauro, Prasad P.W. Appukuttan and Nilesh M Shirode for synthesis, as well as the skilled support of Carsten Bauer for radiolabeling; Luca Gianolla for the QWBA study, Catherine Huck for flow cytometry, Dr. Grazyna Wieczorek for providing cryosections of human tonsils and Dominique Fehlmann for in vitro autoradiographies.

Keywords: Immunology • imaging agents• kinases • radiochemistry • ligand design

References:

[1] For some recent examples, see e.g. a) S. J. Finnema, N. B. Nabulsi, T. Eid, K. Detyniecki, S.-F. Lin, M.-K. Chen, R. Dhaher, D. Matuskey, E. Baum, D. Holden, D. D. Spencer, J. Mercier, J. Hannestad, Y. Huang, R. E. Carson, *Sci. Transl. Med.* **2016,** *8(348)*, 348ra96; b) A. M. Walji,, E. D. Hostetler, H. Selnick, Z. Zeng, P. Miller, I. Bennacef, C. Salinas, B. Connolly, L. Gantert, M. Holahan, S. O'Malley, M. Purcell, K. Riffel, J. L. Jaume Balsells, J. A. OBrien, S. Melquist, A. Soriano, X. Zhang, A. Ogawa, S. Xu, E. Joshi, J. Della Rocca, F. J. Hess, J. Schachter, D. Hesk, D. Schenk, A. Struyk, K. Babaoglu, T. G. Lohith, Y. Wang, K. Yang, J. Fu, J. L. Evelhoch, P. J. Coleman, *J. Med. Chem.* **2016**, *59(10),* 4778-4789; c) J. Li, X. Zhang, Xiang, H. Jin, J. Fan, H. Flores, J. S. Perlmutter, Z. Tu, *J. Med. Chem.* **2015** *58(21),* 8584-8600; d) S. D. Krämer, T. Betzel, L. Mu, A. Haider, A. M. Herde, A. K. Boninsegni, C. Keller, M. Szermerski, R. Schibli, B. Wünsch, S. M. Ametamey, *J. Nucl. Med.* **2018** *59(4)*, 698-703; e) M. Martin-Facklam, F. Pizzagalli, Y. Zhou, S. Ostrowitzki, V. Raymont, J. R. Brasic, N. Parkar, D. Umbricht, R. F. Dannals, R. Goldwater, D. F. Wong, *Neuropsychopharmacology* **2013**, *38(3)*, 504-512.

[2] a) P. Sharma, A. Mukherjee. *Ann Transl Med.* **2016**, *4(3)*, 53; b) C. L. Charron, A. L. Farnsworth, P. D. Roselt, R. J. Hicks, C. A. Hutton, *Tetrahedron Lett.* **2016**, *57(37),* 4119-4127; c) G. Malviya, T. K. Nayak. *Curr Pharm Biotechnol*, **2013**, 14, 669-682.

[3] See e.g. K. Yanamoto, K. Kumata, M. Fujinaga, N. Nengaki, M. Takei, H. Wakizaka, R. Hosoi, S. Momosaki, T. Yamasaki, J.Yui, K. Kawamura, A. Hatori, O. Inoue, M.-R. Zhang, *Nucl. Med. Biol* **2010**, *37(7)*, 853-860, and references cited therein.

[4] Y. Tan, J. Liang, D. Liu, F. Zhu, G. Wang, X. Ding, C. Han, *Exp. Ther. Med.* **2014**, *8(1)*, 69-72.

[5] R. A. Juergens, K. A., A. Singnurkar, D. P. Snider, J. F. Valliant, K. Y. Gulenchyn, *Biomark. Cancer* **2016**, *8(Suppl 2)*, 1-13.

[6] A. D. Fesnak, C. H. June, B. L. Levine, *Nat. Rev. Cancer* **2016**, *16*, 566–581.

[7] F. E. Turkheimer, G. Rizzo, P. S. Bloomfield, O. Howes, P. Zanotti-Fregonara, A. Bertoldo, M. Veronese, *Biochem. Soc. Trans*. **2015**, *43(4),* 586-592.

[8] a) L. Vivash, T. O'Brien, *J Nucl Med* **2016**, *57(2),* 165-168. b) S. Venneti, B. J. Lopresti, C. A. Wiley, *Prog. Neurobiol.* **2006**, *80*, 308–22;

[9] a) A. H Jacobs, B. Tavitian, INMiND consortium, *J. Cereb. Blood Flow Metab.* **2012**, *32(7),* 1393–1415; b) P. Charbonneau, A. Syrota, C. Crouzel, J. M. Valois, C. Prenant, M. Crouzel, *Circulation* **1986**, *73*, 476-483 .

[10] a) M. Imaizumi, E. Briard, Z. S. Sami, J. P. Gourley, J. Hong, Y. Fujimur, V. W. Pike, R. B. Innis, M. Fujita, *NeuroImage* **2008**, *39(3),* 1289-98; b) W. C. Kreisl, M. Fujita, Y. Fujimura, N. Kimura, K. J. Jenko, P. Kannan, J. Hong, C. L. Morse, S. S. Zoghbi, R. L. Gladding, S. Jacobson, U. Oh, V. W. Pike, R. B. Innis, *NeuroImage* **2010**, *49(4)*, 2924-2932.

[11] D. R. Owen, A. J. Yeo, R. N. Gunn, K. Song, G. Wadsworth, A. Lewis, C. Rhodes, D. J. Pulford, I. Bennacef, C. A. Parker, P. L. StJean, L. R. Cardon, V. E. Mooser, P. M Matthews, E. A. Rabiner, J. P. Rubio, *J. Cereb. Blood Flow Metab.* **2012**, *32(1)*: 1–5.

[12] P. R. Territo, J. A. Meyer, J. S. Peters, A. A. Riley, B. P. McCarthy, M Gao, M Wang, M A. Green, Q.-H. Zheng, G. D. Hutchins, *J. Nucl. Med.* **2017**, *58*, 458–465.

[13] R. Tavaré, M. N. McCracken, K. A. Zettlitz, F. B. Salazar, T. Olafsen, O. N. Witte, A. M. Wu, *J . Nucl. Med*. **2015**, *56(8),* 1258-1264.

[14] R. W. Kinne, F. Emmrich, M. Freesmeyer, *J. Nucl. Med. Mol. Imaging* **2010**, *54*, 629-638.

[15] R. Tavaré, M. N. McCracken, K. A. Zettlitz, S. M. Knowle, F. B. Salazar, T. Olafsen, O. N. Witte, A. M. Wu, *Proc. Natl. Acad. Sci. USA* **2014**, *111(3),* 1108-1113.

[16] C. Palmer, M. Diehn, A. A. Alizadeh, P. O. Brown. *BMC Genomics* **2006**, 7, 115

[17] C. Wu, C. Orozco, J. Boyer, M. Leglise, J. Goodale, S. Batalov, C.L. Hodge, J. Haase, J. Janes, J.W. Huss 3rd, A. Su, *Genome Biol.* **2009**, *10(11)*, R130.

[18] E. Montague, I. Janko, L. Stanberry, E. Lee, J. Choiniere, N. Anderson, E. Stewart, W. Broomall, R. Higdon, N. Kolker, E. Kolker, *Nucleic Acids Res.* **2015**, *43*, D1145-51.

[19] Y. P. Auberson, E. Briard, D. Sykes, J. Reilly, M. Healy, *ChemMedChem* **2016**, *11*, 1415;

[20] a) L. Zhang, A. Villalobos, *EJNMMI Radiopharm Chem* **2016** *1(1)*,13; b) G. C. Van de Bittner, E. L. Ricq, J. Hooker, *Acc. Chem. Res.* **2014**, *47(10)*, 3127–3134; c) L. Zhang, A. Villalobos, E. M. Beck, T. Bocan, T. A. Chappie, L. Chen, S. Grimwood, S. D. Heck, C. J. Helal, X. Hou, J. M. Humphrey, J. Lu, M. B. Skaddan, T. J. McCarthy, P. R. Verhoest, T. T. Wager, K. Zasadny, *J. Med. Chem.*, **2013**, *56(11)*, 4568–4579.

[21] J.-M. Jimenez, D. Boyall, G. Brenchley, P.N. Collier, C.J. Davis, D. Fraysse, S.B. Keily, J. Henderson, A. Miller, F. Pierard, L. Settimo, H.C. Twin, C.M. Bolton, A.P. Curnock, P. Chiu, A.J. Tanner, S. Young, *J. Med. Chem.* **2013**, *56(5)*, 1799-1810.

[22] D.C.Brookings, M.C. Hutchings, B.J. Langham, PCT Int. Appl. WO2009093008 A1, 30 Jul. 2009.

[23] N. Gray, T. Zhang, N.P. Kwiatkowski, WO2014063068 A1, 24 Apr. 2014.
[24] J.D. Burch, K. Barrett, Y. Chen, J. DeVoss, C. Eigenbrot, R. Goldsmith, M. H. Ismaili, K. Lau, Z. Lin, D.F. Ortwine, A. A. Zarrin, P. A. McEwan, J. J. Barker, C. Ellebrandt, D. Kordt, D. B. Stein, X. Wang, Y. Chen, B. Hu, X. Xu, P. W. Yuen, Y. Zhang, Z. Pei, *J. Med. Chem.* **2015**, *58(9)*, 3806-16.
[25] F. Brookfield, J. Burch, R.A. Goldsmith, B. Hu, K. Hon Luen Lau, C.H. Mackinnon, D.F. Ortwine, Z. Pei, G. Wu, P.-W. Yuen, Y Zhang, WO2014023258 A1, 13 Feb. 2014.
[26] M. Kaur, M. Singh, O. Silakari, *Cell. Signalling* **2014**, *26(11)*, 2481-92.
[27] Z. Jiang, J. Reilly, B. Everatt, E. Briard, *J. Pharm. Biomed. Anal.* **2011**, *54(4),*722-9
[28] J. D. Burch, K. Lau, J. J. Barker, F. Brookfield, Y. Chen, Y. Chen, C. Eigenbrot, C. Ellebrandt, M. H. Ismaili, A. Johnson, D. Kordt, C. H. MacKinnon, P. A. McEwan, D. F. Ortwine, D. B. Stein, X. Wang, D. Winkler, P. W. Yuen, Y. Zhang, A. A. Zarrin, Z. Pei, *J. Med. Chem.* **2014,** *57(13)*, 5714-27
[29] A. Burchat, D.W. Borhani, D.J. Calderwood, G.C. Hirst, B. Li, R.F. Stachlewitz, *Bioorg. Med. Chem. Lett.* **2006**, *16*, 118–122.
[30] D.J. Calderwood, D.N. Johnston, R. Munschauer, P. Rafferty, *Bioorg. Med. Chem. Lett.* **2002**, *12*, 1683–1686.
[31] J. D. Harling, A. M. Deakin, S. Campos, R. Grimley, L. Chaudry, C. Nye, O. Polyakova, C. M. Bessant, N. Barton, D. Somers, J. Barrett, R. H. Graves, L. Hanns, W. J. Kerr, R. Solari, *J. Biol. Chem.* **2013**, *288(39)*, 28195-28206.
[32] B. N. Cook, J. Bentzien A. White, P. A. Nemoto, J. Wang, C. C. Man, F. Soleymanzadeh, H. H. Khine, M. A. Kashem, S. Z. Kugler Jr., J. P. Wolak, G. P. Roth, S. De Lombaert, S. S. Pullen, H. Takahashi, *Bioorg. Med. Chem. Lett*. **2009**, *19(3)*, 773-777.
[33] Ligand efficiency: a useful metric for lead selection. A. L. Hopkins, C. R. Groom, A. Alex, *Drug Disc. Today* **2004**, *9(10)*, 430-431.
[34] P. Druekes in High Throughput Screening: Methods and Protocols, Methods in Molecular Biology, Issue 1439, (Ed.: William P. Janzen), Springer Science + Business Media, New York, USA, **2016**, pp.143-157.
[35] Ullberg, S. in: O Alvefeldt (Ed.), Special Issue on Whole-Body Autoradiography, Science Tools, LKB Instrument journal, Bromma, Sweden, **1977**, pp. 2-29.

Entry for the Table of Contents

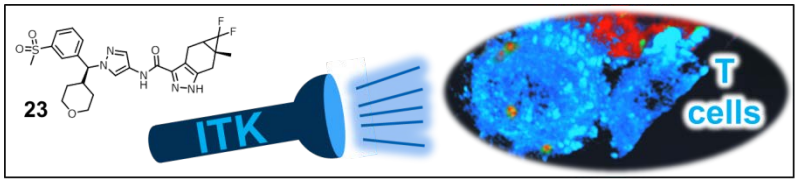

Illuminating T cells in vivo. Four kinases were selected as potential targets for imaging T cell populations by Positron Emission Tomography (PET). Ultimately, the optimization of Itk inhibitors allowed the identification of **23** which, once radiolabeled, proved capable of quantifying T cell concentrations in vivo. This indicates that PET imaging agent that bind to Itk might ultimately allow measuring the distribution of T cells in patients.